Science of the Total Environment 998 (2025) 180256

Contents lists available at ScienceDirect

Science of the Total Environment

journal homepage: www.elsevier.com/locate/scitotenv

A novel and scalable flood risk assessment framework for cultural heritage based on unmanned aerial vehicle photogrammetry and multi-scale rain-on-grid hydraulic modeling

M.J. Alexopoulos [a,*], T. Iliopoulou [a], P. Modé [b], D. Istrati [a,c], C.C. Spyrakos [d], S. Soile [e], S. Verykokou [e], C. Ioannidis [e], D. Koutsoyiannis [a]

[a] Department of Water Resources and Environmental Engineering, School of Civil Engineering, National Technical University of Athens, 15780 Athens, Greece
[b] Institute of Structural Analysis and Antiseismic Research, School of Civil Engineering, National Technical University of Athens, 15780 Athens, Greece
[c] Leichtweiß Institute for Hydraulic Engineering, Faculty of Architecture, Civil Engineering and Environmental Sciences, Technical University of Braunschweig, Germany
[d] Laboratory for Earthquake Engineering, School of Civil Engineering, National Technical University of Athens, 15780 Athens, Greece
[e] Laboratory of Photogrammetry, School of Rural, Surveying and Geoinformatics Engineering, National Technical University of Athens, 15780 Athens, Greece

HIGHLIGHTS

- Nested rain-on-grid links a 5 m island grid to a 0.8 m site mesh, improving depth and velocity estimates at Aegina, Greece.
- Centimeter-resolution UAV photogrammetry supplies the DSM that captures topography governing local pooling and flow routes.
- The workflow relies on freely available HEC-RAS and low-cost drones, making it transferable to other heritage sites.
- Limestone modeling shows compressive-strength loss and stiffness drop after a 24 h inundation, pinpointing vulnerable zones.

GRAPHICAL ABSTRACT

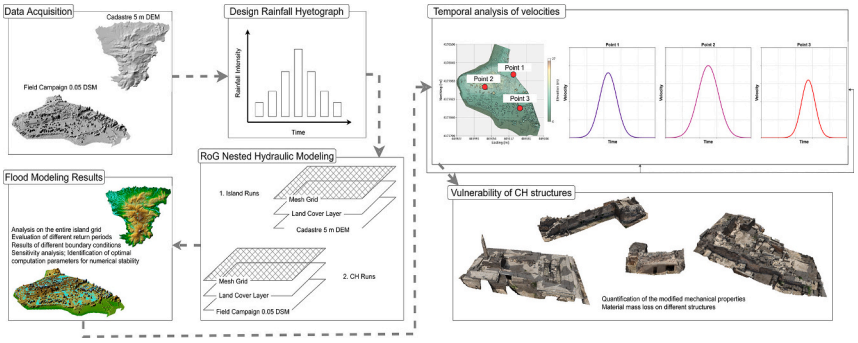

ARTICLE INFO

Keywords:
Flood risk
Computational hydraulics
Photogrammetry
Heritage
Structures
Material degradation
HEC-RAS

ABSTRACT

This study presents a novel multi-scale flood risk assessment framework for cultural heritage sites, applied to the Temple of Apollo, Aegina Island, Greece. Three modeling configurations were developed and compared: (i) an island-wide Rain-on-Grid (RoG) hydraulic model at 5 m resolution, (ii) a site-only model driven by inflows from the island-scale simulation, and (iii) a high-resolution nested model coupling island-scale outputs with centimeter-scale site RoG simulations enabled by UAV photogrammetry.

Simulations for 100-, 1000-, and 2000-year return periods revealed strong scale-dependent differences: island-wide inundation extents of 7.3–10.3 km^2, site-specific inundation of 2–24 %, and water volumes of 92–1483 m^3 depending on the model configuration and return period. Flow velocities remained below 1.0 m/s, indicating low erosive potential but possible material degradation. Limestone deterioration analysis showed 4–10 % compressive strength reduction, 3–9 % elastic modulus decrease, and mass losses of 0.64–26.08 kg after 24-h inundations.

* Corresponding author.
E-mail address: mjalexopoulos@mail.ntua.gr (M.J. Alexopoulos).

https://doi.org/10.1016/j.scitotenv.2025.180256
Received 28 May 2025; Received in revised form 10 August 2025; Accepted 11 August 2025
Available online 22 August 2025
0048-9697/© 2025 The Authors. Published by Elsevier B.V. This is an open access article under the CC BY license (http://creativecommons.org/licenses/by/4.0/).

The nested approach provided more realistic water volume accumulation over the single-scale model and revealed critical micro-topographic controls on flood behavior. This scalable, built on readily accessible tools (HEC-RAS and UAV), framework supports rapid deployment to heritage sites globally, enabling quantitative risk assessments for adaptation planning and conservation prioritization.

1. Introduction

Flooding represents a pervasive geohazard engendered by hydro-meteorological extremes, climatic oscillations, and anthropogenic perturbations of hydro-geomorphic regimes (Cea and Costabile, 2022). Recent catastrophic flood events, namely the May 2023 Emilia-Romagna and October 2024 Valencia inundations, exemplify the spatial extent and socio-economic ramifications of such phenomena, as they precipitate mass evacuations, profound fiscal impacts, and numerous fatalities. Beyond direct structural impacts, floods compromise critical infrastructure networks and fracture social-service continuity (Roldán-Valcarce et al., 2023). Moreover, poor land-use planning and insufficient disaster mitigation measures frequently compound losses, as limited drainage capacity and morphological constraints heighten exposure in both rural and peri-urban areas (Andreadis et al., 2022).

Research on Cultural Heritage (CH) threatened by extreme weather events commenced scholarly discourse in 2003 and by 2015, had expanded to encompass architecture, built environments, climate science, natural hazards and archaeology (Fatorić and Seekamp, 2017). More than a decade ago, UNESCO highlighted water as a key agent of weathering in Europe, compounded by wind-driven rain, airborne salts, and freeze-thaw cycles. Progressive baseline shifts such as sea-level rise, permafrost thaw, and desertification amplify acute impacts, shift environmental baselines and increase floods, droughts, and heatwaves (Sesana et al., 2021). For example, shifting precipitation and temperature–humidity regimes can intensify processes such as crystallization, metal corrosion, and structural destabilization (Sesana et al., 2021). At larger spatial scales, high-resolution hazard mapping is critical for locating the most exposed assets, as demonstrated in mainland Portugal (Figueiredo et al., 2020). For instance, 200-year scenarios can inundate Florence's historic districts (Arrighi et al., 2018) with damage patterns recalling those of the 1966 flood (Pereira et al., 2016).

Modeling capabilities have evolved in tandem. The freely available Hydrologic Engineering Center's River Analysis System (HEC-RAS) platform now includes a two-dimensional Rain-on-Grid (RoG) scheme (Hariri et al., 2022; Iliopoulou et al., 2023), that integrates rainfall–runoff and hydraulics within a single solver and proves advantageous where micro-topography and drainage morphologies dominate flow propagation (Ennouini et al., 2024). Yet RoG accuracy is sensitive to DEM resolution: coarser grids attenuate peaks and distort water levels (Rocha et al., 2020), with predictive skill deteriorating most sharply between 1 m and 5 m (Alexopoulos et al., 2024). Simultaneously, photogrammetry and computer-vision advances enable sub-centimeter 3-D documentation that supports hazard assessment and rapid post-disaster surveys (Blanch et al., 2023), including fluvial- and pluvial-flood contexts (Ben Moshe and Lensky, 2024; Zazo et al., 2018). For CH, Structure from Motion-Multi View Stereo pipelines, UAV imagery and dense point-cloud generation deliver detailed DSMs that refine hydraulic simulations at modest cost (Colucci et al., 2024), and demonstrate improved flood predictions (Vulliet et al., 2024).

Complementing hydraulic studies, ongoing research is also investigating the impacts of water on building materials, with laboratory experiments showing limestone, the main building fabric of the Temple of Apollo in Aegina, —could lose up to 55 % compressive strength under full saturation.

Scale-sensitive complexities persist. Flood-hazard models react strongly to land-use representation and rainfall uncertainty at catchment scale (Pavesi et al., 2024); at meter or sub-meter scale, mesh-size choice and field observations become decisive (Bermúdez and Zischg, 2018; Kumar et al., 2025). Islands introduce further challenges; scale dependent vulnerabilities emphasize the need for integrated modeling frameworks that can effectively bridge large-scale hydrological processes with sub-meter hydraulic simulations (Ioannidis et al., 2024).

To address the scale-dependent limitations outlined above, recent studies have proposed integrated frameworks that align engineering approaches with stakeholder priorities for CH protection. A grounded-theory analysis of Italy's Po River flood-risk plan mapped 13 first-order codes, six themes and three aggregate dimensions—data, knowledge and stakeholders— and put forward a qualitative self-assessment tool to help authorities track progress across assets and governance scales (Arosio et al., 2024). A 2024 review synthesized more than a decade of work into 22 flood-vulnerability indicators grouped in five themes—construction geometry, material properties, building envelope, flood-emergency planning and site context—clarifying the state of knowledge while noting that most empirical evidence still comes from European case studies (Salazar et al., 2024a). Snelling et al.'s Heritage Building Flood Robustness Toolkit couples component-level flood-damage scoring with a six-step Structured Decision-Making workflow that lets owners weight robustness, aesthetics and operability when ranking retrofit options (Snelling et al., 2024). Ginzarly et al. advance this integration by linking landscape-scale flood-hazard layers with 23 socio-economic indicators, then showing that 55 % of flooded households lie in statistical units where cultural-heritage vulnerability is already highest, underscoring the equity stakes of CH protection (Ginzarly et al., 2024). Erbach widens this debate by showing that CH can be mobilized as a multifunctional resource for adapting to weather extremes—delivering informational, emotional, economic and community-building benefits across engineered, technological and educational measures, and thereby steering flood-risk work toward a more holistic resilience agenda (Erbach, 2025).

Taken together, such advances mark a maturing—yet still fragmented—state of practice. Indicator catalogues and socio-spatial dashboards now span scales from basin to brick. Yet the multi-scale framework introduced in the present study is the first to integrate catchment-scale hydrological modeling (inflows) with centimeter-scale monument hydraulics and to propagate those flows into stone-level deterioration maps by bridging the gap between hydrological sciences, computational hydraulics, material science, risk engineering and CH. Importantly, this approach is packaged in freely available tools that respective stakeholders can directly incorporate into site-management plans and investment prioritization.

2. Study area

The study focuses on the Temple of Apollo, a CH site located on the island of Aegina in Greece (Fig. 1). It is situated in the Saronic Gulf, approximately 20 km southwest of Athens, and covers 82 km^2. The Temple of Apollo, positioned on the island's north-western part, holds historical significance as an archaeological site dating back to the Classical period.

The archaeological site of the Temple of Apollo is situated along the coast with a steep cliff to the west. The site was originally a prehistoric settlement comprising an inner core and eastern suburb. Abandoned around 1200 BCE, it later became an Iron Age necropolis and flourished from the Archaic to Roman periods. From the 6th to the 10th century CE, the site was home to a large Byzantine settlement. Excavations have taken place since the 19th century. Restoration efforts began in the

1970s, focusing on the inner suburb walls, while the outer suburbs remained unprotected until 2015. Prolonged exposure of numerous prehistoric-to-Archaic walls, causing structural weakening. A significant restoration campaign was launched in 2011 and prioritized backfilling and consolidating the walls using scientifically approved mortars, particularly in the western area, where Byzantine-era structures remain threatened by maritime traffic and erosion, increasing the risk of collapse.

As is customary, the ancient stone foundations of the Temple lack modern drainage infrastructure, and combined with local depressions, this can cause water to pool during heavy rain. The surrounding vegetation, while contributing to soil stabilization, may enhance the effect of pooling by retaining moisture and slowing drainage, thereby exacerbating damp conditions and potentially accelerating the degradation of the stone material.

The surrounding area is characterized by low-lying topography and limited natural drainage, making it susceptible to flood-related risks. Aegina's elevation ranges from sea level to approximately 532 m, with the study area falling within the lower elevation zones near the coastline (Fig. 2). The island is characterized by limited urban development, with built-up areas constituting approximately 6 % of its total land area.

The region's climate is Mediterranean, with mild, wet winters and dry summers. Land use within the study area includes sparse vegetation, small-scale agricultural plots, and archaeological excavation areas. Impermeable surfaces are minimal but concentrated around the immediate vicinity of the temple. While annual rainfall on the island is generally low, the unique characteristics of the cultural site—its proximity to the sea, low-lying topography, and absence of proper drainage infrastructure—exhibit a potential vulnerability to flood risk, which warrants further investigation into the local hydrological challenges.

3. Methodology

3.1. Framework

The methodological framework of this study comprises various stages, as summarized in Fig. 3, to systematically integrate field data acquisition and hydrological/hydraulic modeling at the catchment and local scale. Each step is detailed below.

3.2. Photogrammetric data acquisition and processing

The campaign for photogrammetric data acquisition for the Temple of Apollo and the surrounding area in Aegina took place on June 25, 2024 (snapshots of the field survey can be found in the supplementary material). A DJI Mavic 3 Enterprise drone was initially used, capturing 945 nadir images to achieve complete site coverage. To ensure high-resolution documentation of architectural elements, including slopes, walls and intricate structural details, an additional dataset of 4900 oblique images were acquired by the same drone at lower altitudes. Furthermore, a DJI Mavic 2 Pro drone was utilized to capture 930 images of areas in the archaeological site, mainly surrounding the Temple of Apollo. The distribution of the images captured by both drones is depicted in Fig. 4.

Additionally, 15 pre-marked Ground Control Points (GCPs) were strategically placed around the site and measured using a Leica 1200 (Global Navigation Satellite System) (GNSS) receiver in the Greek Geodetic Reference System (GGRS ‘87). The Networked Transport of RTCM via Internet Protocol Real-Time Kinematic method was applied to receive real-time corrections via the MetricaNet GNSS permanent station network. Finally, 10 additional characteristic points within the site were surveyed. The GCP distribution is depicted in Fig. 5.

The photogrammetric processing was carried out using the Agisoft Metashape Professional software (Agisoft, 2025), following a Structure-from-Motion (SfM) – MVS pipeline.

The initial stage involved the estimation of the interior and exterior orientation parameters for all ~6700 images and the generation of a sparse point cloud containing ~2.4 million points. This process comprises several steps, including the automatic detection of overlapping image pairs, feature extraction and image matching, feature tracking and the main SfM methodology. The georeferencing of the SfM results was based on the GCP measurements (15 GCPs), while additional check points were measured to assess the positional accuracy. The resulting root mean square (RMS) error was ~4 cm for the GCPs and ~ 6 cm for

Fig. 1. Temple of Apollo in Aegina.

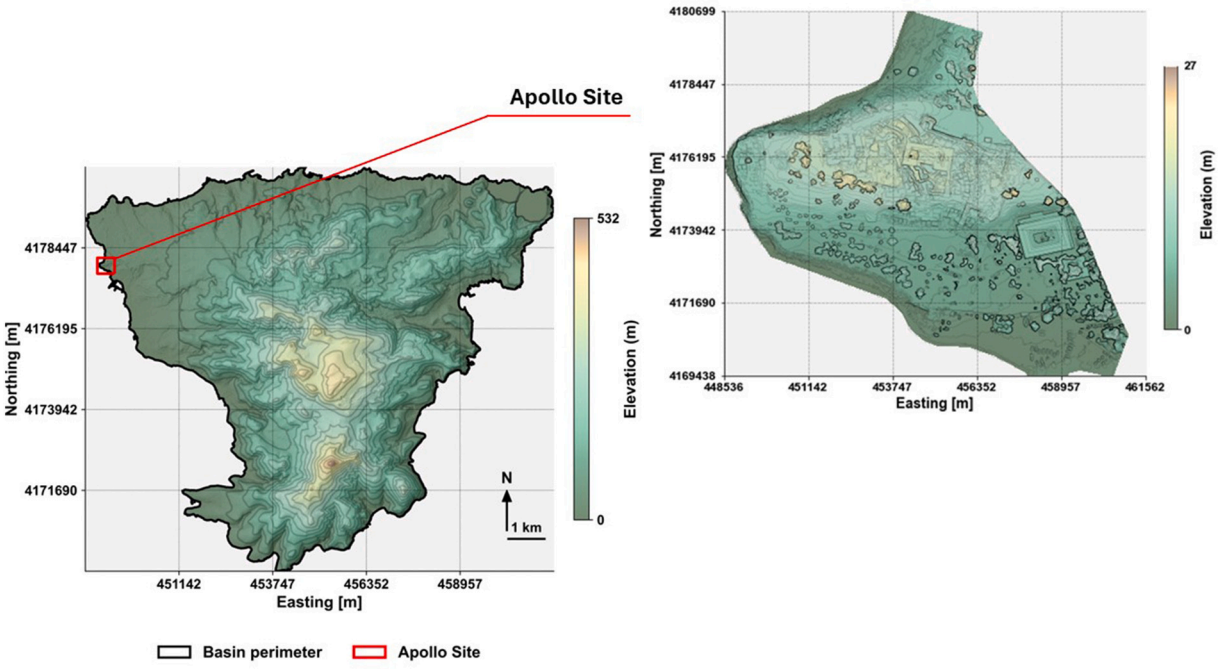

Fig. 2. Study area elevation and location. Illustration of the Aegina modeling perimeter, in addition to the site of the Apollo Temple. Elevation resolutions are 5 m for the island, and 0.05 m for the Apollo Site.

the check points.

Following this, the dense point cloud of the study area was generated. This step involves (i) executing dense image matching for overlapping image pairs with known interior and exterior orientation parameters, leading to the creation of depth maps for the reference images, and (ii) converting these depth maps into 3D points by projecting them into space to reconstruct the dense point cloud.

The final step was the generation of the study area DSM, using the produced 3D dense point cloud.

3.3. Design hyetographs

Design rainfall curves are a common tool in hydrological design and flood risk assessment. The curves define the relationship between rainfall intensity, the timescale, and the return period. This relationship enables engineers to estimate design rainfall events for a given location. In this study, the probabilistic model for design rainfall over Greece is based on the revised methodology of Iliopoulou et al. (2024). The model relates the rainfall intensity x (in mm/h), the timescale k (in hours), and the return period T (in years) as follows:

$$x = \lambda_* \cdot \frac{\left[\left(\frac{T}{\beta_*}\right)^{\xi} - 1\right]}{\left(1 + \frac{k}{\alpha}\right)^{\eta_*}} \tag{1}$$

where:

$\alpha = 0.18$ h and $\xi = 0.18$ (dimensionless) are applied uniformly across the country, and

λ_* (mm/h), β_* (years), and η_* (dimensionless) vary spatially (Iliopoulou et al., 2024).

These spatial parameters are derived from a grid with a 5 km resolution covering the entire country. The mean-representative point rainfall curve for each catchment is then obtained by performing an area-weighted averaging of the grid parameters within a Geographic Information System environment. For the study area, the catchment-specific parameter values are $\lambda_* = 67.60$ mm/h, $\beta_* = 0.020$ years, and $\eta_* = 0.72$.

For a given return period e.g., 100 years, design rainfall events are constructed using the Alternating Blocks method. In this approach, the total rainfall depth is partitioned into several sectional depths (blocks), which are arranged sequentially in time. The maximum depth is placed at the center of the event, with the remaining blocks allocated alternately in descending order to the left and right of the center.

Design rainfall events are constructed for a total duration of 24 h—a period chosen to be sufficiently longer than the catchment's concentration time (considering the island-wide region). The intensities provided by Eq. (1) correspond to point rainfall. However, hydrological analyses typically require catchment-average surface intensities. To convert point intensities to surface intensities, an Areal Reduction Factor (ARF) is applied. The ARF for time scales ranging from 1 min to 25 days and for areas between 1 and 30,000 km^2 is expressed as follows:

$$\varphi = \max\left\{1 - \frac{\left[0.048 \cdot A^{0.36 - 0.01 \cdot \ln(A)}\right]}{k^{0.35}}, 0.25\right\} \tag{2}$$

where:

A is the area in km^2, and

k is the timescale in hours.

The procedure described above produces a design rainfall event based on the specified duration and return period. However, it is the soil's infiltration capacity that ultimately determines how much of the rainfall becomes surface runoff—this portion is known as the active or excess rainfall. To estimate infiltration losses and separate them from the total hyetograph, the method developed by the US Soil Conservation Service is used. This method is based on the following assumptions:

- During an initial period, denoted as t_{a_o}, all rainfall during this time, ha_o, is absorbed entirely as a deficit (initial deficit), resulting in no excess runoff. Therefore, after this time ta_o, the maximum effective rainfall depth cannot exceed h- ha_o where h represents the total rainfall depth of the event.
- Beyond the initial deficit, h_{a_o}, the additional deficit during heavy rainfall cannot exceed a maximum value known as potential maximum retention, denoted as S. The initial deficit is expressed as $ha_o = 0.1S$. A decreased value of 0.1 instead of the textbook 0.2 has

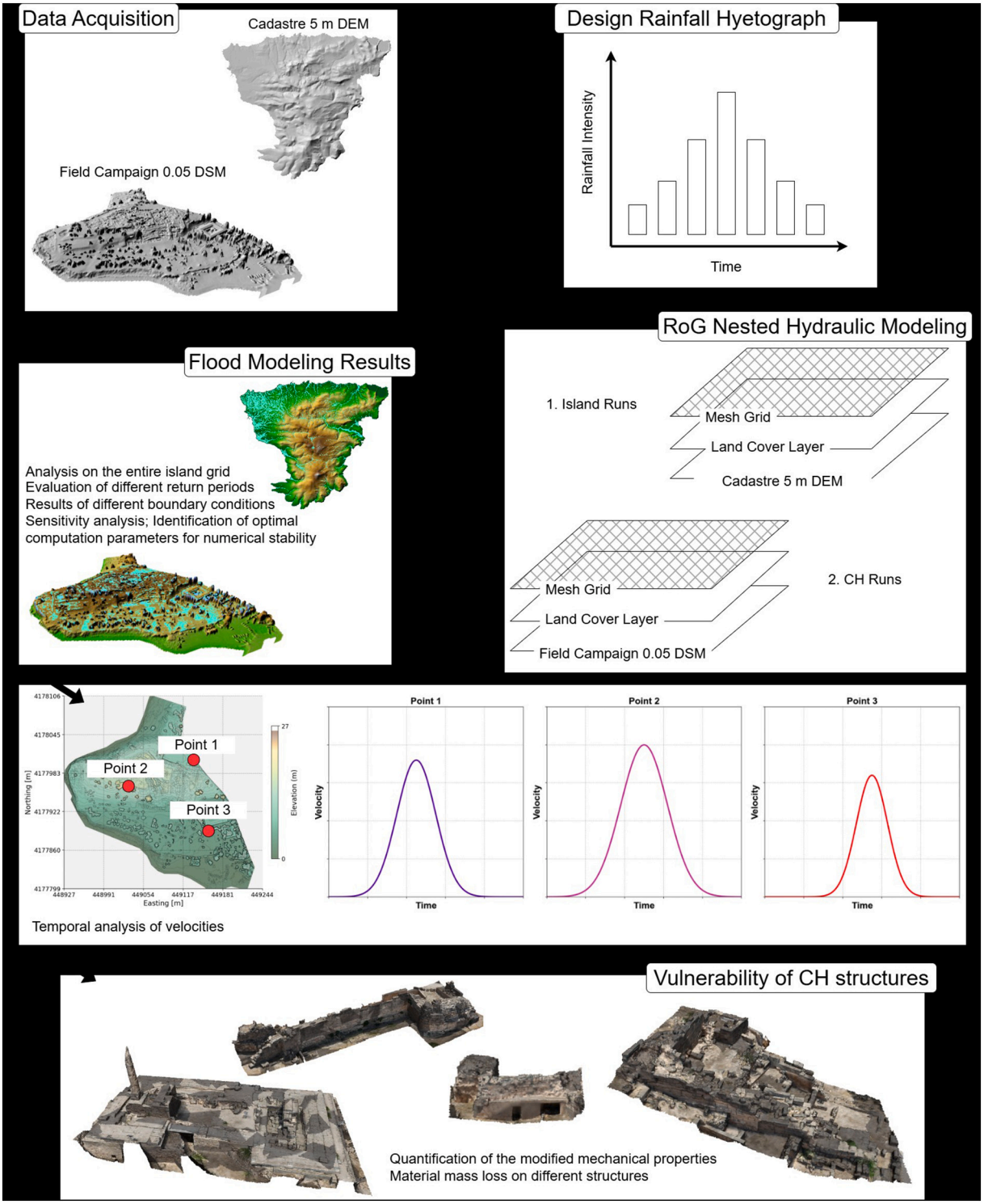

Fig. 3. Schematic of the multi-tiered methodological paradigm.

been chosen. The change has been for consistency with literature findings, because a study in the same region found that the actual initial abstraction ratio was significantly lower than 0.2, with an average ratio of just 0.014 for an entire catchment and 0.037 for a sub-catchment (Baltas et al., 2007). Therefore, adopting an initial abstraction ratio of 0.1 represents a more realistic yet conservative approach.

- For any time, $t > t_{a_o}$, the ratio of the excess rainfall depth to the additional deficit (ha- h_{a_o}) is equal to the ratio of these values to their potential counterparts (h-ha_o) and S, respectively. Based on these assumptions, the following empirical equation is used to estimate the excess rainfall:

$$h_e = \begin{cases} 0, & h \le 0.1S \\ \dfrac{(h-0.1S)^2}{h+0.9S} & h > 0.1S \end{cases} \quad (3)$$

Eq. (3) is applied both to the total rainfall depth and to partial (block) rainfall depth values, allowing the temporal evolution of the event to be determined. The above formulation is the classic SCS Curve-Number (CN) method; in this study we modify it in two ways: (i) we apply the runoff equation block-wise to derive a time-distributed excess-rainfall

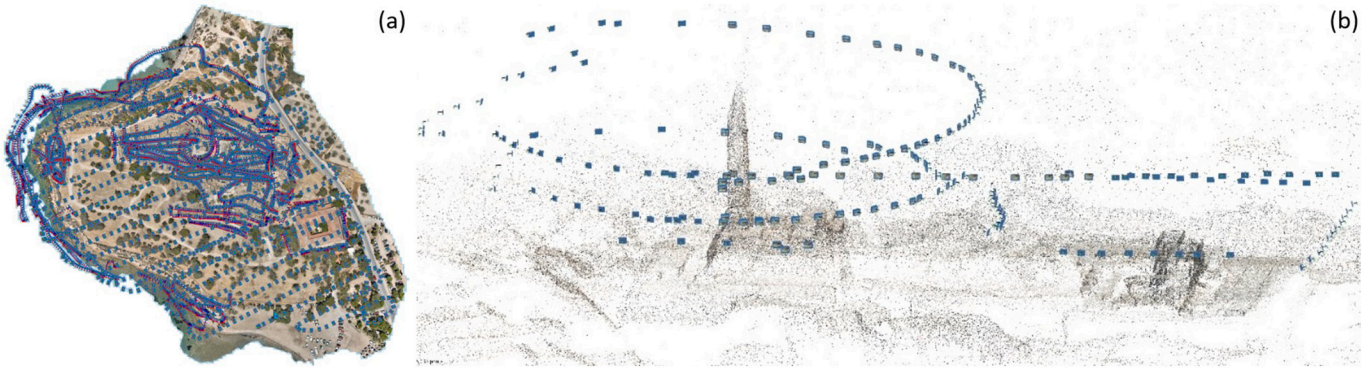

Fig. 4. Schematic illustration of the flight paths for the distribution of the vertical and oblique images captured by the DJI Mavic 3 Enterprise drone over the produced 3D model of the area (a) and schematic illustration of the distribution of the images captured by the DJI Mavic 2 Pro drone over the sparse point cloud of the archaeological site of the temple of Apollo (b).

Fig. 5. Distribution of the GCPs measured in the archaeological site of the Temple of Apollo, superimposed on the textured 3D model of the site. CH angle from North to South.

hyetograph compatible with the RoG solver, and (ii) we adopt an initial-abstraction of 0.10 as it is more appropriate. All other steps follow the standard CN procedure during model computation. The deficit depth can asymptotically approach 1.1S for large rainfall events. If runoff data is unavailable CN, the parameter S can be estimated from existing literature. Specifically, S (in mm) is linked to the runoff, which is a key parameter describing the catchment. The relationship between S and CN is given by:

$$S = 254\left(\frac{100}{CN} - 1\right) \tag{4}$$

The CN value ranges from 0 to 100 and is determined by factors such as soil type, land use, and antecedent moisture conditions in the catchment. Here, a layer of CN values is used derived from the European Space Agency's land cover typology.

3.4. Rain-on-grid hydraulic modeling

HEC-RAS, developed by the United States Army Corps of Engineers (USACE), is a widely utilized tool for hydraulic simulations due to its open-source nature, reliable numerical solvers and continuous updates. Recent advancements in HEC-RAS include using measured or remotely sensed rainfall data as a spatially distributed boundary condition, a technique commonly known as RoG approach. Unlike traditional methods, which rely on pre-computed runoff hydrographs generated by external hydrological models, RoG integrates rainfall-runoff processes directly within the hydraulic model. The approach lets rainfall be applied uniformly or spatially varied across the domain, enabling a more cohesive simulation of rainfall-runoff dynamics and flood propagation (Hariri et al., 2022).

HEC-RAS 2D offers multiple computational methods, including the Diffusion Wave Equations and two forms of the Shallow Water Equations

(SWE): SWE-ELM (Eulerian-Lagrangian Method) and SWE-EM (Eulerian Method). The SWE-EM solver employs a finite difference approach to solve the two-dimensional shallow water equations. Derived under the shallow-water assumption (horizontal scales ≫ vertical), they form a set of hyperbolic partial differential equations that describe the conservation of mass and momentum in surface water flows. As described by Hariri et al. (2022), these equations can be expressed in the following two-dimensional forms:

Continuity Equation (Mass Conservation)

$$\frac{\partial h}{\partial t} + \nabla(Vh) = q \tag{5}$$

Momentum Equation

$$\frac{\partial V}{\partial t} + (V\nabla)V = -g\nabla(h+z) + \mathrm{v_t}\nabla^2\mathrm{V} - \mathrm{c_f}V \tag{6}$$

In these equations:

h represents water depth.

V is the velocity vector.

q accounts for water balance terms such as rainfall and infiltration.

g is gravitational acceleration.

ν_t is the horizontal eddy viscosity coefficient.

z is the bed elevation.

S_f is the slope of bottom friction.

When terms related to viscosity and advection are neglected, the equations reduce to the simpler Diffusion Wave approximation:

$$\frac{\partial \boldsymbol{V}}{\partial t} + g\nabla(h+z) = gS_f \tag{7}$$

The equations are solved over the computational mesh, with boundary conditions specified at catchment edges and hydraulic structures. Numerical stability demands compliance with the Courant–Friedrichs–Lewy (CFL) condition. The Courant number Cr is a key parameter, expressed as:

$$Cr = \frac{u\Delta t}{\Delta s} \tag{8}$$

where:

u is the characteristic wave propagation speed.

Δt is the computational time step.

Δs is the spatial discretization length.

Stability of explicit time-integration schemes is governed by the Courant–Friedrichs–Lewy criterion ($\mathrm{Cr} \leq 1$). While implicit methods and specific solver configurations may allow for slightly higher Courant numbers, maintaining Cr close to or below unity is generally recommended to avoid numerical instability and oscillations. Fine-tuning the Courant number according to terrain, flow conditions, and grid resolution through iterative adjustments ensures stable and accurate hydraulic simulations.

Both the island and CH runs were designed to maintain a Courant number within acceptable ranges, limiting the likelihood of numerical instabilities. By initializing a 15 s base step with iterative halving, the solver enforces $Cr \leq 1$, automatically reducing Δt upon any violation, to preserve numerical stability across rapid flow transients. The final selection of these stability-related parameters was guided by diagnostic checks (e.g., simulation logs, spot checks of velocity profiles) rather than relying solely on preset values.

3.5. Coupling catchment-scale and site-scale simulations

A two-dimensional (2D) hydraulic model was constructed to represent the entire island domain, leveraging the aforementioned 5 m resolution DEM provided by the Greek Cadastre. The island-scale model simulates large-scale overland flow and the upstream runoff that may reach the CH site.

We executed dual simulation paradigms: (i) a CH run driven solely by the island run hydrograph (Fig. 7); and (ii) a nested RoG run, in which the upstream hydrograph is superimposed with on-grid rainfall forcing.

Our approach is used to compare the inundation extents and volume differences around the peak time of rainfall. Regarding the computational mesh, HEC-RAS employs a sub-grid method that computes detailed elevation profiles along each cell face instead of assigning one uniform elevation per cell. This means that even with larger grid cells, critical topographic features, such as levees and banks, are accurately captured, provided the cell boundaries represent those features well. To balance computational efficiency with spatial fidelity, the primary mesh discretization was configured at 25 m, with a nested refinement overlay in the northwestern sector contracting cell dimensions to 5 m. To guarantee numerical stability, the CH-site mesh is further refined to 0.8 m.

Three modeling configurations were prepared to compare spatial fidelity and computational cost. To identify the most suitable modeling approach, we tested three cases. The first approach included an island-wide model with the CH site included, the second one focused only on the CH site with inflow conditions from the island-wide model, and the third approach was a multi-scale one, where the results of RoG hydraulic analyses of an island-wide model (5 m resolution) were used as boundary conditions in RoG analyses of a high resolution model of the CH site only (0.05 m resolution).

3.6. Sensitivity to halving base timestep strategy (T100, T2000)

A sensitivity analysis was performed to stabilize the CH run driven by the island-run boundary condition and the RoG inputs for the 2000-year event (chosen as an extreme event to stress-test the stability of the model). Multiple simulations were performed with incremental changes in these parameters until achieving a satisfactory result that ensured model outputs, particularly velocity, remained free of spurious oscillations. Additional simulations were conducted, incrementally increasing the halving step parameter from 1 to 3 and 4. The parameter regulates the magnitude of Δt attenuation during simulations. Although the selected initial time-step was already short relative to conventional catchment-scale studies, further refinement was necessary. For example, starting with a base time step of 15 s, one halving step reduces the time step to 7.5 s (doubling the number of computational steps for a one-hour simulation from 240 to 480), and two halving steps reduce it further to 3.75 s (960 steps). The doubling effect follows a geometric progression—often referred to as exponential scaling—which significantly increases the computational burden. The simulation adopted four halving steps ($\Delta t = 3.75$ s), as justified in Section 4.3.

3.7. Mechanical deterioration induced by flood water

The central structure of the Aegina archaeological site is the Temple of Apollo, which is constructed from ‘tufa’, a yellowish limestone native to the island. Due to the lack of available laboratory testing, the material properties of this limestone could not be directly determined. As a result, standard values were used in analyses to assess the deterioration of limestones' mechanical properties.

Two mechanical quantities were studied to approach the durability of limestone. Equations 9and 10 were used to identify the deterioration in compressive strength and elastic module, respectively. These equations were obtained from Li et al. (2022). The results of the aforementioned study demonstrated a clear correlation between saturation duration and reductions in compressive strength and stiffness. The following empirical relationships were proposed:

$$\sigma_c = 71.32 - 7.86t + 0.43t^2 \tag{9}$$

$$E = 44.67 - 4.24t \tag{10}$$

where σ_c is the uniaxial compressive strength in MPa, E is the elastic

modulus in GPa, and t is the water saturation time in days.

3.8. Mass deterioration of material from flood water

Flood events are significant hydrological phenomena that can dramatically accelerate limestone deterioration due to both mechanical and chemical processes, as mentioned earlier in this study. Such events subject limestone to intense water flow and pressure, exacerbating its decay. Experimental studies have investigated this topic, revealing a clear relationship between inundation time and the rate of mass loss in limestone (Fan et al., 2022). In these studies, the mass loss rate was defined as the percentage of the initial dry mass lost due to water exposure. The remaining mass of a specimen was calculated using the following relation (Miao et al., 2016):

$$m_{r,t} = m_0 - \eta \cdot m_0 \tag{11}$$

where $m_{r,t}$ is the remaining mass of the structure after exposed to water for t days, m_0 is the initial mass and η is the rate of mass loss (100 %). While the absolute mass loss varied among different specimens, the progression of mass loss followed consistent trends under the same pressure conditions. However, significant differences were observed under varying pressure levels, as the pressure directly influences the mass loss rate (Fan et al., 2022).

This rate is experimentally linked to dynamic pressure, as illustrated in a graph by Fan et al. (2022). The pressure increases substantially during flood events due to the rising velocity of flowing water, sometimes reaching several meters per second in extreme events. The dynamic pressure exerted on limestone structures can be estimated using the following expression derived from fluid dynamics:

$$P_d = \frac{\rho v^2}{2} \tag{12}$$

where P_d is the dynamic pressure (Pa), ρ is the density of water (approximately 997 kg/m^3), v is the velocity of the flowing water (m/s). This dynamic pressure represents the kinetic energy of the moving water acting upon limestone surfaces and can induce mechanical stresses that lead to erosion, surface detachment, and enhanced chemical weathering through prolonged saturation.

While Eq. 12 provides a theoretical approximation, actual pressures may exceed these values under turbulent flow conditions or in the presence of localized effects such as cavitation or high-velocity jet impacts. The emphasis of this study on flow dynamics captures the primary forces driving limestone degradation during floods.

Moreover, limestone's inherent porosity enables water to infiltrate beneath the surface, allowing hydraulic pressure to act internally. This internal pressure, coupled with surface impacts, promotes both surface and subsurface deterioration. Factors such as surface roughness and porosity influence how the pressure is absorbed and distributed, potentially generating additional pore pressure within the rock. These internal stresses further compromise the mechanical integrity of limestone, making it especially vulnerable during high-intensity flood events.

4. Results

4.1. Photogrammetric products

Three-dimensional documentation of the Temple of Apollo precinct yielded a sub-centimeter–accurate dense point cloud and derivative DSM. The resultant point cloud (≈61 × 10^6 points; point cloud can be seen in the supplementary material) affords granular surface characterization. The DSM, produced using the aforementioned dense point cloud, provides a detailed representation of the terrain; it has a resolution of 5 cm and depicts the site's elevation variations across a 30 m range; it is illustrated in Fig. 8.

In addition to UAV-derived products, fifteen island-wide DEM tiles (Greek Cadastre) were integrated (visual representation of the procedure can be seen in the supplementary material) to support regional-scale analyses.

4.2. Island run outcomes

Inundation extent undergoes a gradual amplification with more extended return periods (Fig. 9), particularly in the low-lying regions on the north-western part of the island, where the CH site is.

For the 100-year event, flood depths remain localized within valley floors and depressions, with minimal propagation into adjacent elevated areas. In contrast, both the 1000-year and 2000-year scenarios illustrate more significant flood impacts; the 1000-year scenario highlighting increased inundation due to topography, while the 2000-year event reaches maximum extent with intensified flow accumulation and expansion into previously unimpacted areas. The inundated areas were calculated to cover 7.3, 9.6 and 10.3 km^2 for the three return periods respectively.

The depth differences between return periods are shown (Fig. 10). The color scale differentiates increases and decreases, with red indicating positive differences and blue indicating negative differences. Due to the difference in extents, depth-variance heterogeneity localizes along the main channels and low-lying areas on the north-western part based on the raster of the smallest return period. As expected, the most pronounced differences appear in the transition from the 100 to 2000-year return period. Depth variations seldom exceed 4 m, as the island is low-lying with minor elevations. Hydraulic connectivity remains largely unhindered due to anthropogenic developments sited at mean sea level.

4.3. Sensitivity to halving base timestep strategy

As discussed in sub-section 3.6, the numerical results are highly dependent on the CFL number, which is affected by the time-step. One way to affect the time-step of the analysis is by using a halving methodology, which allows the solver to reduce the time-step in half during the analysis. A quad-segment snapshot illustrates the numerical-stabilization process to suppress convergence anomalies in the 2000-year return period event simulation (Fig. 11). The three rows depict the max depth, max velocity, and Courant number at 12:00, which corresponds to the peak runoff transformation period, where numerical instabilities are most likely to manifest.

The first row confirms that depth distributions remain consistent across halving steps, with no observable instability-related anomalies. However, the second row highlights a pronounced issue in velocity outputs, where non-realistic values emerge. While post-processing interpolation-induced artifacts were considered, subsequent analysis suggested that the observed discrepancies predominantly arise from numerical instability. The pursuit was made despite the volume accounting error remaining within acceptable thresholds.

A reduction in the Courant number (third row) is observed as the number of halving steps increases, which in turn contributes to a more stable and accurate simulation while depth distributions remain largely unaffected, whereas velocity fields exhibit significant improvements. Notably, water-propagation patterns vary with the chosen Δt. This is consistent with the literature (Kumar et al., 2025), as areas with rapid velocity changes require smaller cell sizes to capture flow dynamics accurately.

4.4. Multi-scale flood assessment at the cultural heritage site

Fig. 12, from left to right, depicts (i) the island-scale inundation footprint extending beyond the DSM coverage, (ii) the CH-run hydrograph-only inundation pattern confined to natural depressions and drainage pathways, and (iii) the nested RoG result showing maximal extent despite negligible depth increments.

Hence, we identify a localized wetting pattern that predominantly aligns with the natural depressions and predefined drainage pathways, which can be captured only by the multi-scale RoG modeling approach. As expected, the flood extent is smaller than in the full-domain run because no on-grid rainfall is applied. We observe the most expansive inundation extent. Although the depths are insignificant, the inundated area expands markedly, especially in zones where micro-topography dictates retention and redistribution.

Although the comparison with the island run is imperfect because different DEMs were used, the resulting wet areas still differ significantly. One contributing factor may be the smoother surface produced by interpolation and averaging. For example, if a 5-m cell blocks an adjacent 5-m cell due to elevation differences, water may not advance as readily (depending on flow conditions) as it would with a higher-resolution DEM. In the latter, micro-topographical features with higher elevations prevent the overall cell surface from being uniformly elevated, allowing more water to flow normally. The straightforward remedy is to use a uniformly high-resolution DEM across the entire hydraulic domain so that micro-topography is preserved in every cell. It is important to note that this issue does not arise in our case. In the simulation using only the hydrograph as a boundary condition for the CH run, water still fails to propagate, and the wetted area is significantly reduced even though rainfall was applied directly to the grid. This reduction is most likely due to the chosen mesh size, as it has been demonstrated that it can alter simulation results with an impact as significant as the roughness parameter (Prior et al., 2024). In addition, coarser mesh size in RoG simulations fail to capture accurately localized variations (Kumar et al., 2025). Thus, for RoG, both the DEM cell size and the mesh size affect not only water routing but also the model's inundation predictions at specific times. As a result, a modeler may miss detecting areas that have become wet, even when using fine timesteps.

The CH runs at 12:00 indicate that incorporating the RoG approach consistently increases both the percentage of inundated areas and the corresponding water volume (Table 1).

For the 100-year return period, the simulation using only island boundary input results in 2 % inundation and 92 m^3, while the addition of RoG raises these values to 3 % and 175 m^3, respectively. Similarly, under the 2000-year return period, the isolated island boundary input yields 20 % inundation and 1211 m^3; with RoG, these figures increase to 24 % and 1483 m^3. Therefore, in all the remaining sections of the paper the multi-scale RoG modeling approach is used.

A quadrant encompassing part of the area where the archaeological monuments are located (Fig. 13 and Fig. 14). The plots indicate that while wetted areas occur within the site as expected, depth and velocity distributions exhibit invariance across return periods. The uniformity arises from (a) limited monument-scale relief confining flow to isolated depressions, and (b) the flat CH-site morphology draining toward peripheral lowlands. Instead, water accumulates within isolated surface depressions, though these are predominantly situated outside the monument zone, particularly in the northern and southern peripheries of the site.

Secondly, the CH area's overall flat topography, combined with its adjacency to lower-elevation zones to the north and south, facilitates runoff migration toward these external depressions. This effect is further substantiated by Fig. 13, which shows preferential water accumulation beyond the immediate monument area, reinforcing the role of external drainage pathways in shaping localized flood behavior.

The difference between velocity and depth spans one order of magnitude (Fig. 15) during the peak of the design rainfall hyetographs, as illustrated previously in Fig. 6. While significant differences in depth are observed across the spectrum, particularly between the 100 and 2000 periods, depth appears relatively more stable compared to velocity. In contrast, velocity exhibits a more uniform variation across the modeled domain. The findings are consistent with expectations for the relatively flat topography of the archaeological part domain of the CH site, with lower velocities in minor slopes and depression areas.

The archaeological core shows the highest inundation frequency, mainly because shallow depressions and gentle slopes impede drainage. As a result, floodwater persists longer in these areas. No significant differences are observed across the different return periods.

Since the flood velocities can play a critical role for soil erosion, scour development and degradation of foundations' stability, Fig. 17 illustrates several sampling locations where velocity profiles were extracted during the CH run, employing boundary conditions from the island run+RoG scenario across all selected return periods.

Fig. 18 displays the corresponding profiles, revealing that although the differences between individual sampling points are significant by an order of magnitude, the overall velocity values remain below 1 m/s, preventing discernible patterns from emerging. Moreover, the variations in the maximum velocities across the different return periods tend to be minimal for most points (except e.g., for point 1), a result attributed to the inherent characteristics of the study site. Since the area does not function as an outlet for the island and does not accumulate substantial water volumes that might induce compounded effects, the CH site essentially behaves as an isolated basin. Its gentle slopes and the absence of abrupt topographical variations further contribute to the consistency observed in the velocity field. For points 3, 8 and 9, velocity peaks occur well before the rainfall peak. This phenomenon can be attributed to localized depressions within the domain where water accumulates; once a certain volume is reached, the water tends to pool rather than continue moving, which leads to these premature velocity peaks. Moreover, it can be observed that for certain locations the more extreme scenarios (1000 and 2000 return period) some locations like points 2 and 5 exhibit noticeable flow velocities for a longer duration.

4.5. Deterioration of limestone

Considering that the inundation time in the archeological site is considerable, it was essential to analyze the deterioration of limestone through these inundation periods. Therefore, the deterioration was assessed in terms of compressive strength and elastic modulus reduction, as well as mass loss, using the mathematical models described in the methodology section. As illustrated in Fig. 16 flooding events range in duration from 0 to 1 day for return periods of 100, 1000, and 2000 years respectively. Table 2 presents the compressive strength and elastic modulus of the limestone, calculated using Eqs. 9 and 10, as well as the deterioration rates for the flood intervals depicted in Fig. 16. According to the table for limestone structures that are inundated during the

Table 1
Percent of inundated area and volume of water for return periods of 100 and 2000 years for the two CH runs.

Run ID	Return period 100 years CH Run 12:00 – Island Boundary Input	Return period 100 years CH Run 12:00 – Island Boundary Input + RoG	Return period 2000 CH Run 12:00 – Island Boundary Input	Return period 2000 CH Run 12:00 – Island Boundary Input + RoG
Parameter				
Percent of inundated area (%)	2	3	20	24
Volume of water (m^3)	92	175	1211	1483

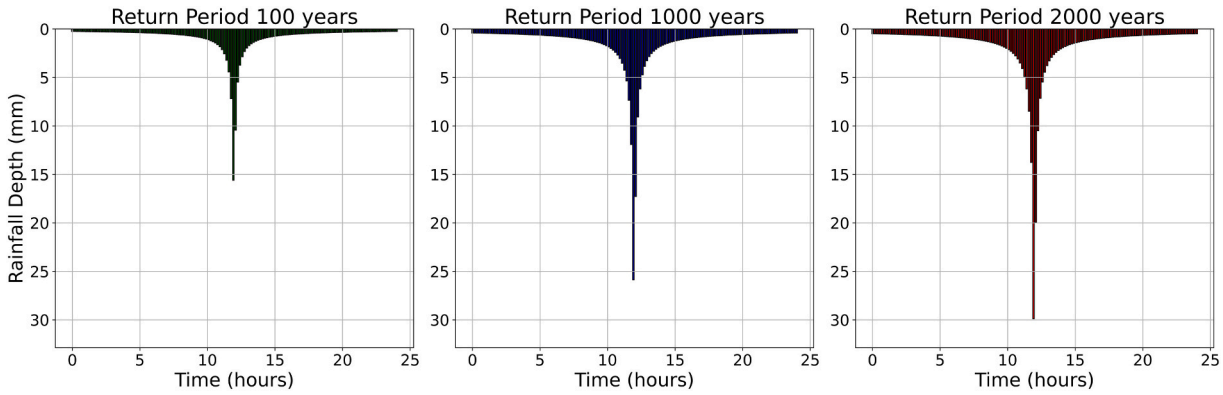

Fig. 6. Design hyetographs for return periods of 100, 1000 and 2000 years.

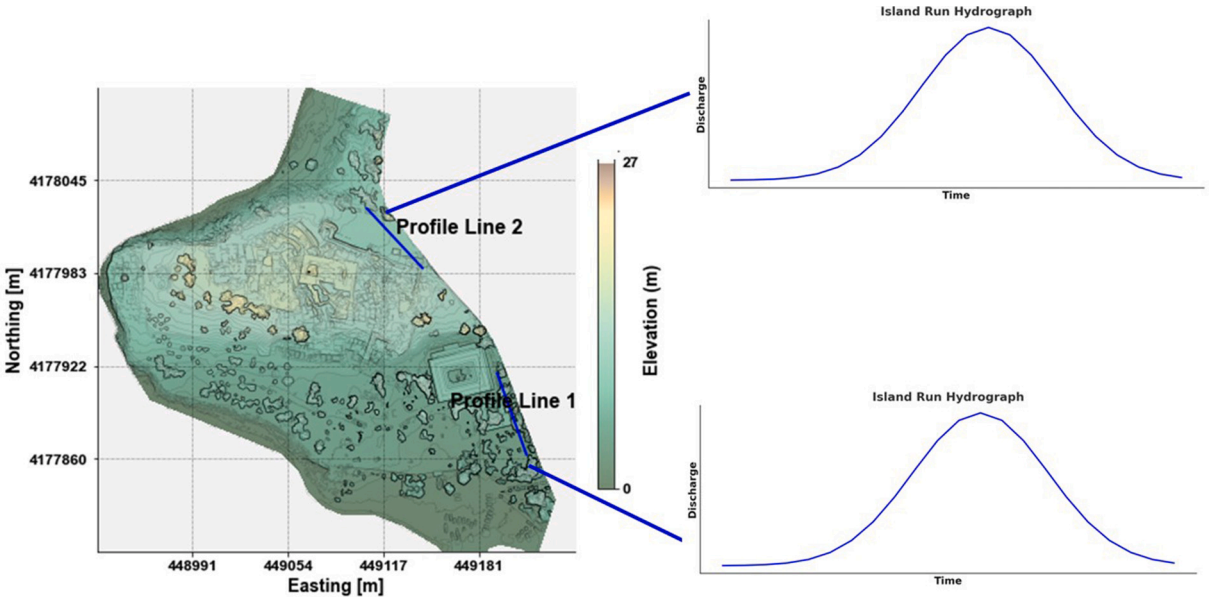

Fig. 7. Location of hydrograph extraction from Island runs for implementation in the CH runs.

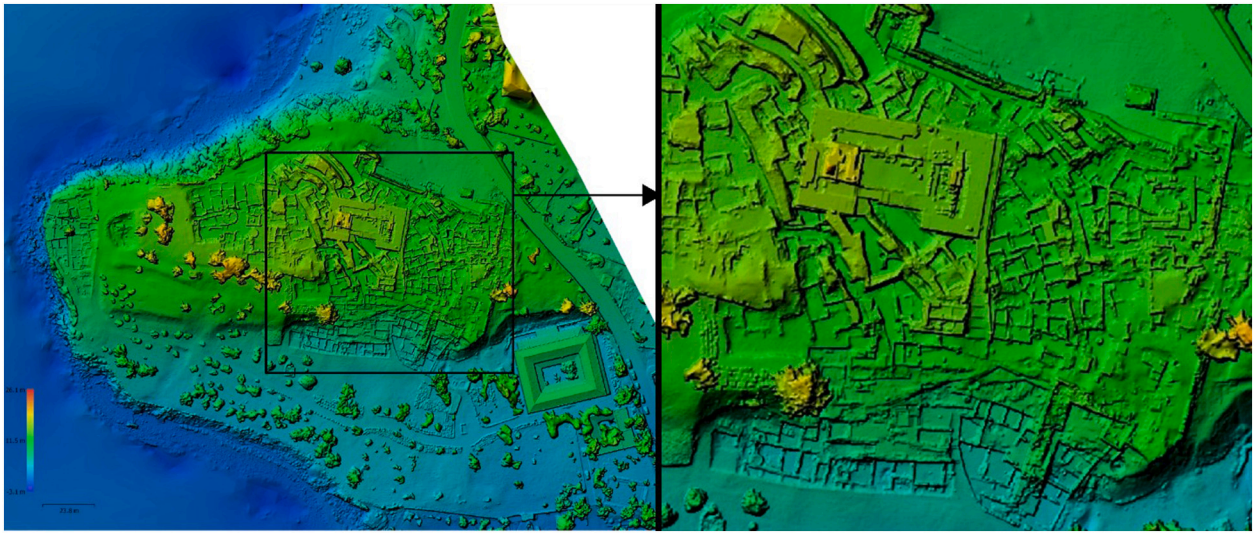

Fig. 8. DSM of the archaeological site of the temple of Apollo and zoom-in view, derived by UAV-based photogrammetry.

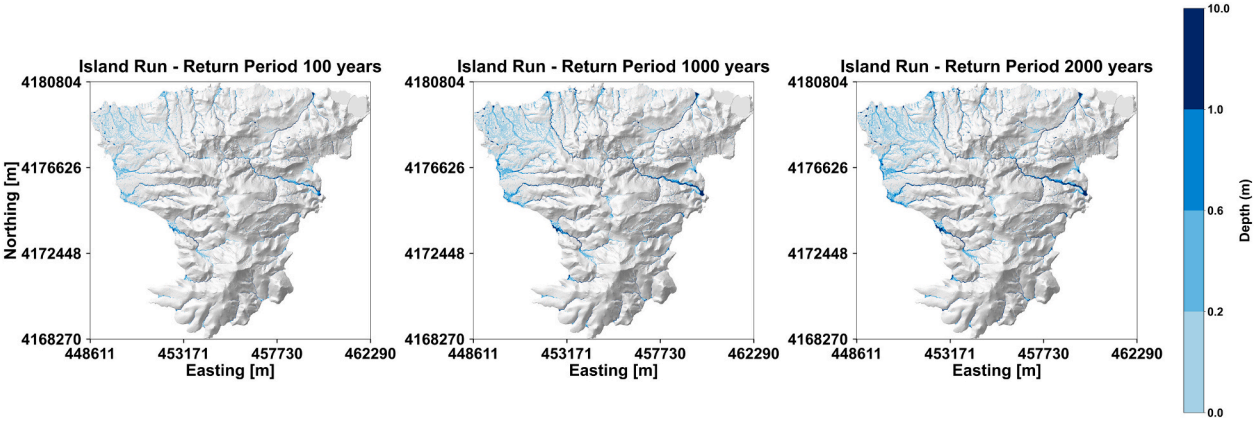

Fig. 9. Maximum inundation depth and spatial extent in island-scale simulations for 100-, 1000-, and 2000-Year return periods.

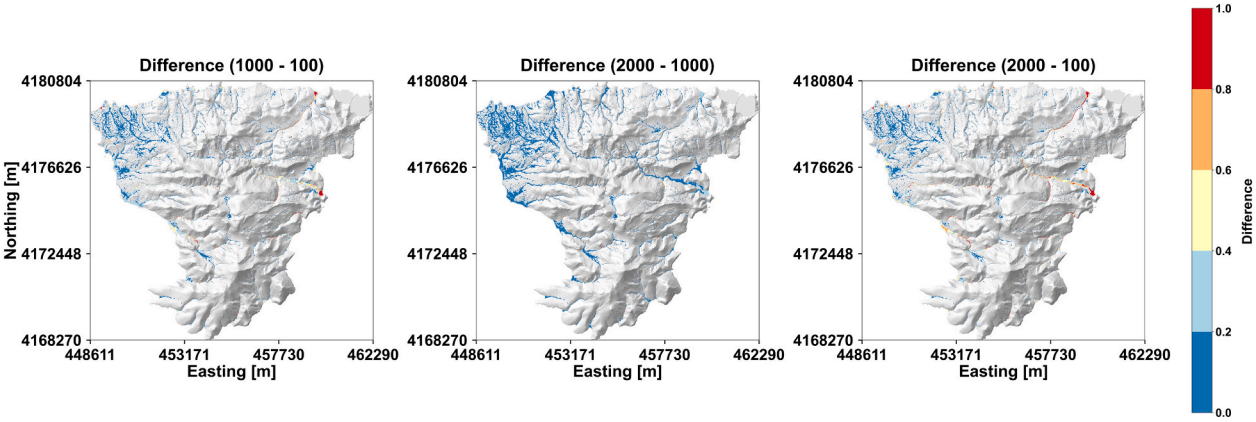

Fig. 10. Depth difference and extent for island runs for 100-, 1000-, and 2000-Year return periods.

flooding event could have a reduction of compressive strength between 4.31 % and 10.42 % when the inundation duration is between 40 % and 100 %, while the reduction of the elastic modulus would be between 3.8 % and 9.49 %.

Fig. 19a illustrates the deterioration rate of compressive strength, categorized according to the inundation classes defined in Fig. 16. Each class, representing a percentage of daily water exposure, is associated with a specific deterioration rate. Similarly, Fig. 19b displays the deterioration rate of the elastic modulus of limestone. Structures deteriorate by the percentages shown on the color bar. A slight but consistent increase in deterioration rates is observed in both figures as the flood return period increases. Notably, the highest rates of deterioration are predominantly concentrated near the summit of the hill, in proximity to the temple, likely due to localized factors.

The last step for the material deterioration assessment is the quantification of material loss, which as explained in section 3, depends on the dynamic pressure. Using Eq. 12, the dynamic pressure P_d is 299 Pa, 698 Pa and 997 Pa for the characteristic velocities of 0.3, 0.7 and 1.0 m/s, respectively. Since the dynamic pressure is relatively low (i.e., less than 1 MPa) for all cases, according to the results of Fan et al. (2022) it can be neglected and the value of dynamic pressure can be assumed equal to 0 MPa (i.e., atmospheric conditions) for the rest of the analysis.

The density values for the dry limestone are taken as 2.65 g/cm^3 (i.e., 2650 kg/m^3) (Vásárhelyi, 2005). As mentioned at the beginning of this section and shown in Fig. 16, the maximum duration of flood events considered, is 24 h, corresponding to a maximum water exposure time of 1 day. Based on this condition and assuming a pressure of 0 MPa, the mass loss rate (η) is estimated to be 0.01 %, as indicated in a graph provided by Fan et al. (2022). This value comes directly from their graph; the authors did not publish an explicit equation.

Table 3 shows the remaining mass at water duration of 1 day ($m_{r,t}$) derived from the deterioration of the limestone using Eq. 11 for selected key structures. The first key structure is the column of the Apollo temple, the second is the base of the column, the third is the short wall opposing the column, and the fourth is the outer wall.

5. Discussion

In the comparative analysis between island-wide and site-level hydraulic simulations conducted herein, the value of combining coarse regional simulations with locally detailed data is clear, as the flood extents differ significantly, especially if we are interested in the centimeter scale (Fig. 12), and computational resources can be a constraint. The island-scale simulation effectively delineates general inundation patterns and provides essential boundary conditions. However, it lacks the resolution required to capture the micro-topographical nuances present at the local scale.

In the literature, it has been shown that many CH sites are situated in inherently vulnerable settings—often in protected lowlands adjacent to tributaries or at topographical knickpoints—where historical urban management practices and evolving anthropogenic pressures exacerbate flood risk (Kim and Sung, 2024). In contrast, high-resolution site-level models incorporating detailed digital surface data enable a more precise characterization of local geomorphological features that could influence the pattern of water propagation and provide more conservative estimates (Brussee et al., 2021).

We see that the nested RoG hydraulic approach offers a distinct advantage over conventional lumped hydrological methods by explicitly

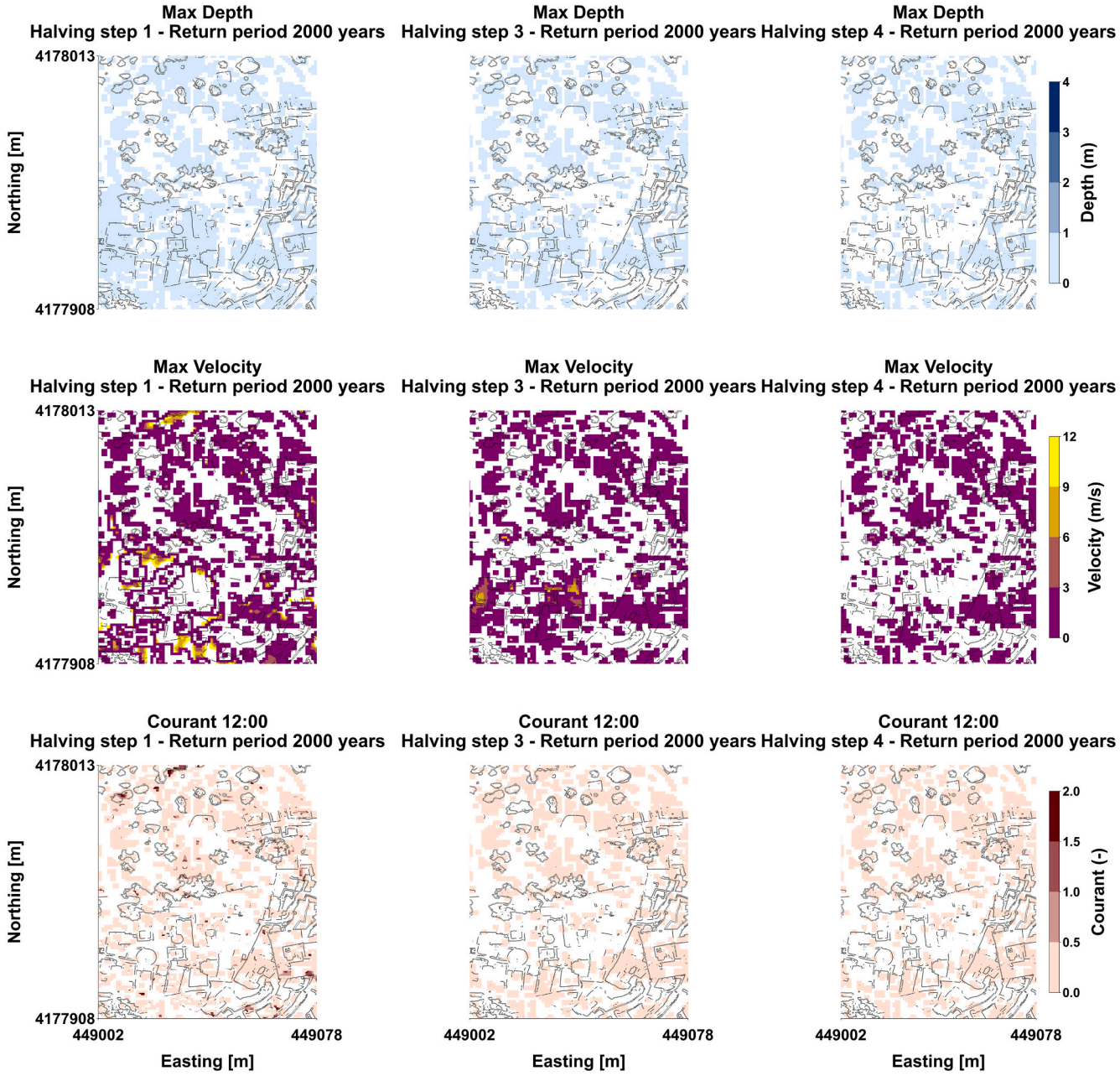

Fig. 11. Stabilization profiles—maximum depth, velocity, and Courant number at peak flow (12:00) for CH sub-domain.

capturing the spatial variability in infiltration and localized pooling. In the RoG framework, as precipitation is directly applied to the computational grid, nuanced representations of spatial heterogeneities are preserved in surface properties and soil infiltration rates. This becomes even more relevant for enhanced spatial resolution in particularly critical regions lacking formal drainage infrastructure, where micro-topographical variations may significantly influence water accumulation and distribution (Fig. 13, Fig. 14). As observed somewhat recently (Giani et al., 2022), even though many rainfall events may exhibit a predominantly uniform pattern at larger scales, the explicit quantification of spatial moments can discern events in which localized variability critically alters the runoff response—an aspect that lumped approaches, relying on averaged hydrographs, tend to oversimplify. Moreover, comparative evaluations of RoG models have demonstrated that HEC-RAS 2D replicates key features of flood hydrographs (notably the recession limb) with greater fidelity than its alternatives, owing to its capacity to integrate sub-grid topographical details (Godara et al., 2024). In addition, uncertainty assessments indicate that while hydrological inputs remain a significant source of variability, the uncertainties related to hydraulic parameterization (such as floodplain roughness) are comparatively lower when employing an explicit grid-based framework (Annis et al., 2020). Consequently, the RoG method—primarily as implemented in HEC-RAS—provides a more reliable depiction of the flood processes by ensuring that critical micro-topographical factors are adequately represented in simulation outcomes.

Implementing fine-resolution simulations inherently demands stringent adherence to numerical stability criteria, particularly those imposed by the CFL condition. While detailed grid discretization enhances the representation of micro-topographic influences, it simultaneously imposes tighter constraints on the solver's time step to preclude

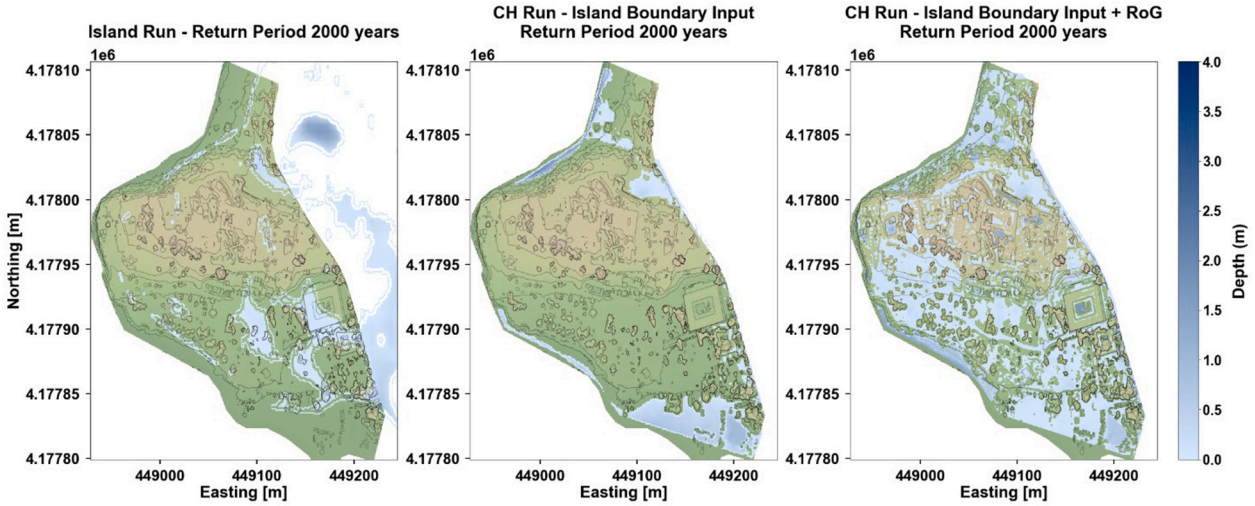

Fig. 12. Comparative maximum water depth and inundation extent for the 2000-year return period: island vs. CH runs.

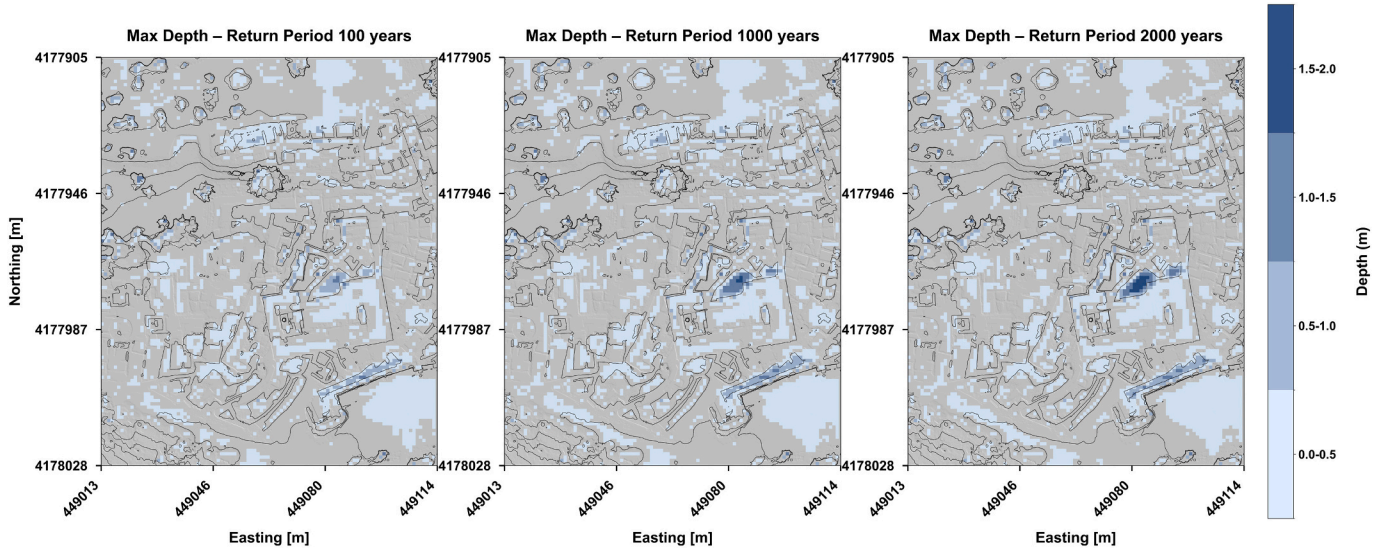

Fig. 13. Depth distribution across the quadrant for 100-, 1000-, and 2000-Year return periods.

the emergence of unrealistic velocity magnitudes. In our study, greater instabilities and pronounced CFL violations were observed in the portions of the modeled area where slope is greater, a pattern that is intuitive and consistent with earlier studies (Alexopoulos et al., 2024). To address these issues, we employed an iterative halving strategy to reduce the Courant number, ultimately setting a target limit of 0.6. This adjustment, together with a variable time step, follows best practice reported in the literature (Guan et al., 2018). Optimization of the time-stepping scheme revealed that the results from the third and fourth halving iterations began to converge, with the fourth iteration providing the most reasonable range of velocity values. Notably, while the maximum flood depth distributions remained relatively invariant across the various time-stepping schemes, the refinement process markedly improved the fidelity of the velocity fields.

Recent studies emphasize the necessity of refining flood risk analyses for CH by integrating high-resolution topographic and hydrological data with empirical damage information. For instance, ex post assessments of flood-damaged heritage sites (De Lucia et al., 2024), have shown that both tangible (e.g., structural material, decorative elements) and intangible (e.g., historic continuity, communal significance) values are susceptible to water depth, velocity proxies such as local river slopes, and suboptimal state of conservation (Salazar et al., 2024b). Nonetheless, we argue that purely large-scale or moderate-resolution modeling often overlooks site-specific traits—such as raised floors, concealed basements, or valuable artworks on lower levels—that amplify vulnerability yet may be captured only via on-site surveys and centimeter-level DSMs, compared to frameworks that suggest it is possible at different scales (Brokerhof et al., 2023). In this regard, our framework, which combines a nested RoG approach with a field campaign, agrees with methods that pair hydrodynamic modeling and post-event field data to elucidate how microtopography and fine-scale drainage pathways could shape flood impacts (Malgwi et al., 2021). By coupling external inflows derived from catchment-wide simulations with local-scale surveys, the procedure may allow for more robust ex-ante vulnerability estimates. It bridges the gap between coarse-grained hazard delineations and the nuanced reality of heritage assets facing physical and non-physical flood-related threats.

The value of this high-resolution perspective extends beyond flood mapping. It is also critical in assessing the deterioration of limestone, as our results reveal a pronounced dependence of degradation patterns on microtopographic variations. Local depressions, flow accumulation zones, and moisture-retaining features, captured only through

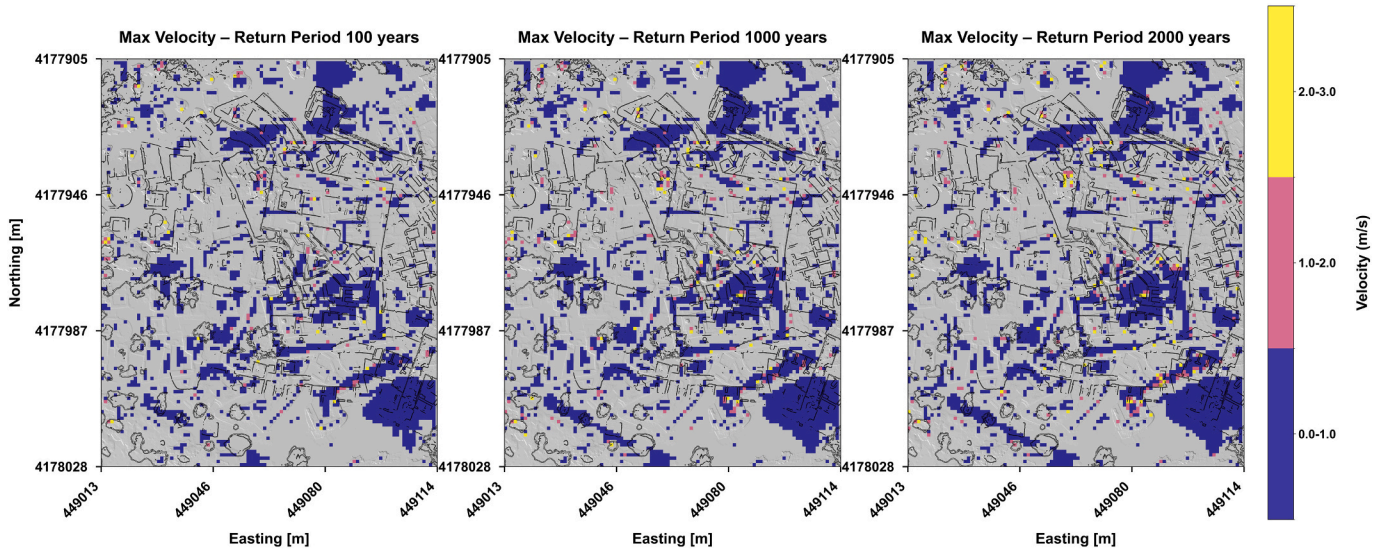

Fig. 14. Velocity distribution across the quadrant for 100-, 1000-, and 2000-Year return periods.

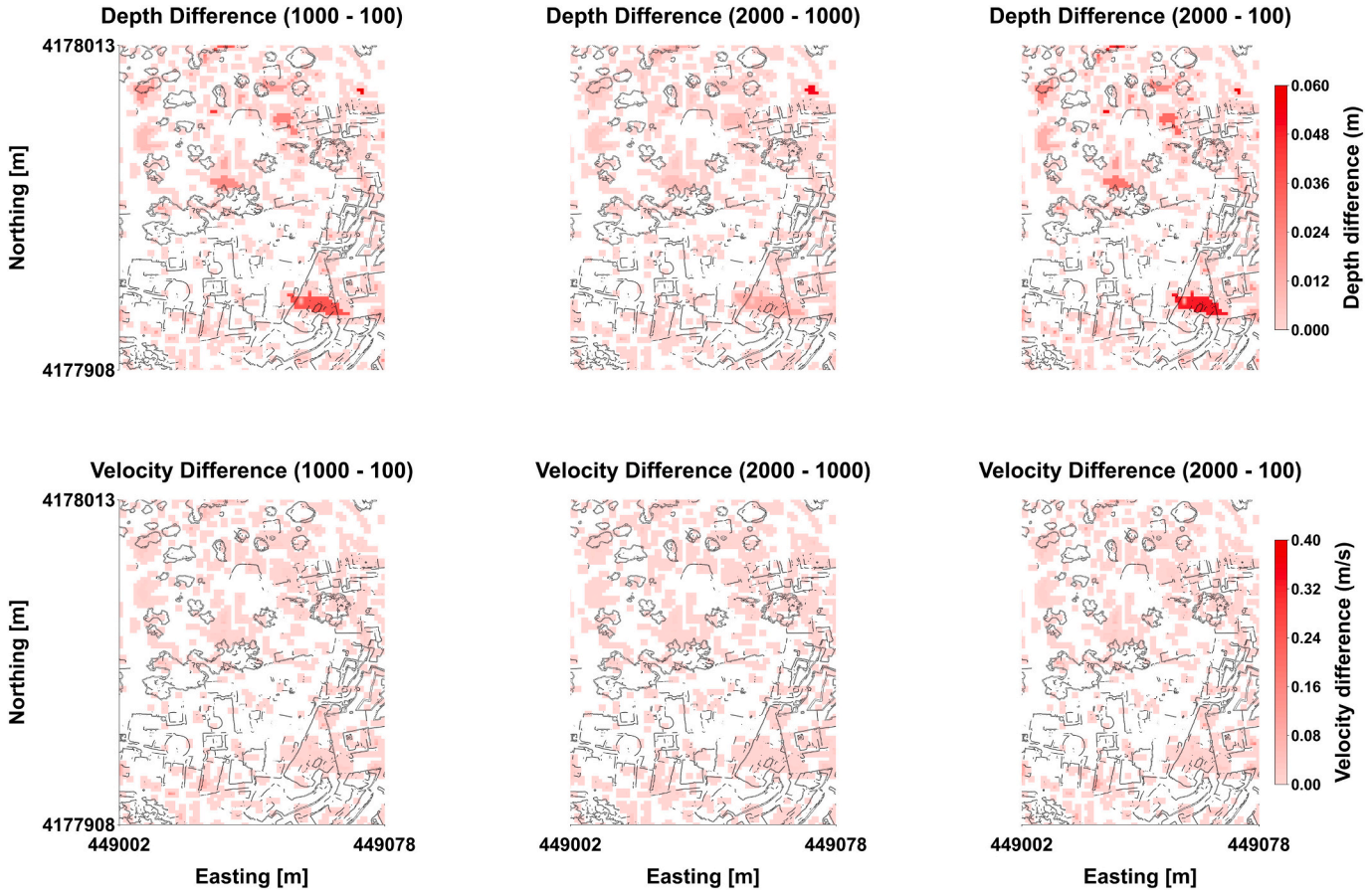

Fig. 15. Depth and velocity difference for CH runs for 100-, 1000-, and 2000-Year return periods at 12:00 profile.

centimeter-scale surface models, can play a pivotal role in accelerating material decay. Beyond the technical gains achieved here, our nested-hydraulics/limestone-decay workflow helps close several gaps flagged in recent CH risk studies. Large-area indicator approaches—such as the modified geographically weighted regression that explained 92.8 % of flood losses at 417 Chinese monuments (Liang et al., 2024) and the Fuzzy-Analytic Hierarch Process, Sentinel-2-based surface that captured >75 % of historic floods around Hoi An's World-Heritage core (Nguyen et al., 2024)—perform well with 10 m inputs but cannot depict sub-meter ponding that controls stone saturation and mechanical decay. In contrast, component-based, depth-only models for single buildings (Figueiredo et al., 2021) resolve façade-level heterogeneity yet still omit flow-velocity and flood-duration terms now included in our RoG-derived limestone maps. Our Aegina results also echo the resolution lessons from

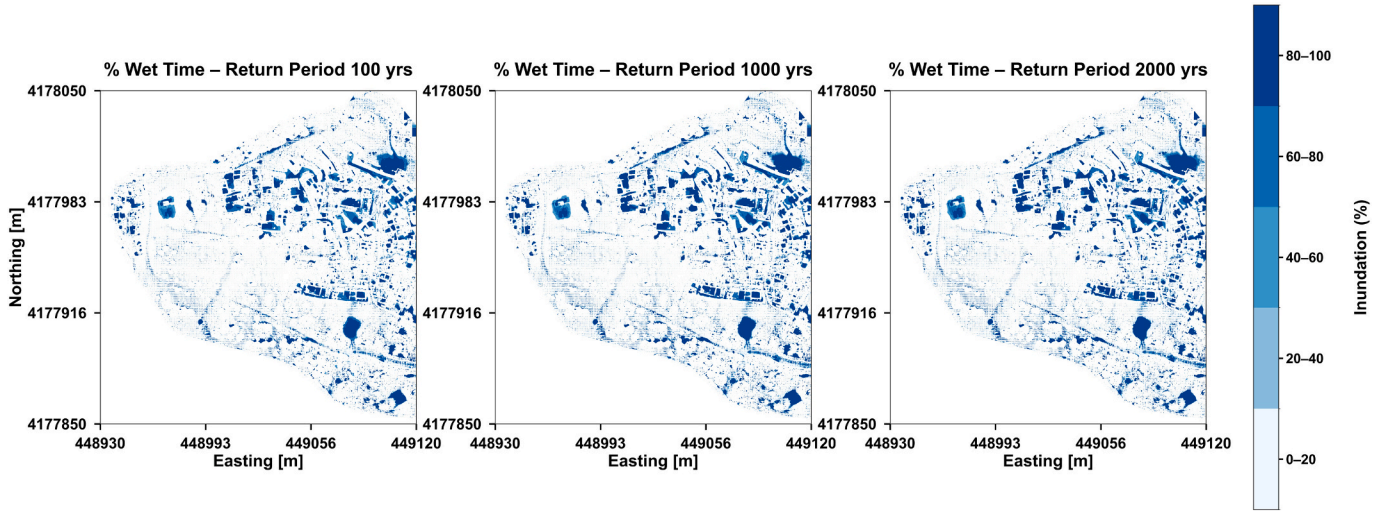

Fig. 16. Percentage of time inundated for 100-, 1000-, and 2000-Year return periods.

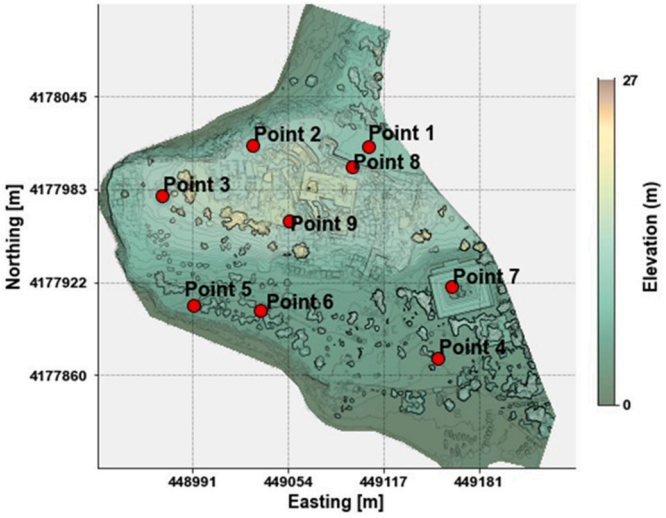

Fig. 17. Sampling locations for velocity profile extraction in CH run.

Florence's Santa Croce study (Tamagnone et al., 2025): a 1 m city-wide DTM proved adequate for street flow, yet bespoke field surveys were still required inside landmark buildings— therefore our decision to employ UAV-derived centimeter DSMs for limestone-critical hollows is reinforced. They further align with multi-hazard findings that anthropogenic change and low-lying micro-topography outweigh broader climate drivers (Wang, 2015); by showing how a 5 m grid can hide limestone-critical depressions, our study supplies a physical rationale for the high AHP weights those authors allocate to land-use and elevation indices. Finally, because we rely on open-source HEC-RAS and low-cost UAV data, the workflow can operate as the intermediate or second-tier layer within multilevel assessments, such as the ones proposed by Figueiredo et al. (2021), or complement the preventive-mapping framework promoted by Wang (2015).

5.1. Limitations and future research

As with any study, some limitations present themselves: While this study establishes a methodological framework for flood risk assessment in CH contexts, comprehensive uncertainty and sensitivity analyses remain areas for future research. Such analyses, although valuable, extend beyond the current study's scope and could be addressed in subsequent work to further refine our proposed approach. The integration of coarse island-scale and high-resolution site data introduces uncertainty in reconciling spatial heterogeneities, which may affect flood propagation accuracy. Numerical instabilities observed during high return period events necessitated iterative time-step adjustments, which limit the generalizability of the model settings. Additionally, the lack of post-event field validation restricts a full assessment of the model's predictive performance.

6. Conclusions

This study developed and applied a two-tier hydraulic modeling framework to assess flood risk at the Temple of Apollo in Aegina. By integrating island-wide RoG simulations with high-resolution photogrammetric data, the approach enabled a detailed characterization of local flow dynamics and inundation patterns at the CH site. Key findings include:

The combination of coarse-resolution regional simulations with site-specific, centimeter-resolution DSM data resulted in significant improvements in capturing localized pooling and hydraulic behavior when compared with runs that relied solely on the 5 m island-wide DEM and hydrograph-based boundary conditions. The use of UAV-derived DSM enhances the reliability of the hydraulic simulations by accurately representing micro-topographic variations, ephemeral drainage features, and potential water pathways. In addition, the RoG method preserves more faithfully the spatial variability of rainfall-runoff processes in contrast to conventional lumped hydrological approaches. Using the proposed multi-scale modeling approach, it was possible to quantify the water levels, flood velocities and inundation duration, not only at the site level but also at the structural component level.

Furthermore, iterative time-step halving notably improves model stability, particularly in the prediction of velocity fields, even though flood depth distributions remain relatively stable. High-resolution photogrammetric data also plays a critical role in identifying subtle topographic features that govern water accumulation and flow redistribution within the CH area. Finally, melding catchment-derived inflows with site-scale modeling reveals discrepancies in inundation footprints, which emphasizes the importance of accurately representing upstream runoff contributions. Although this study employed synthetic

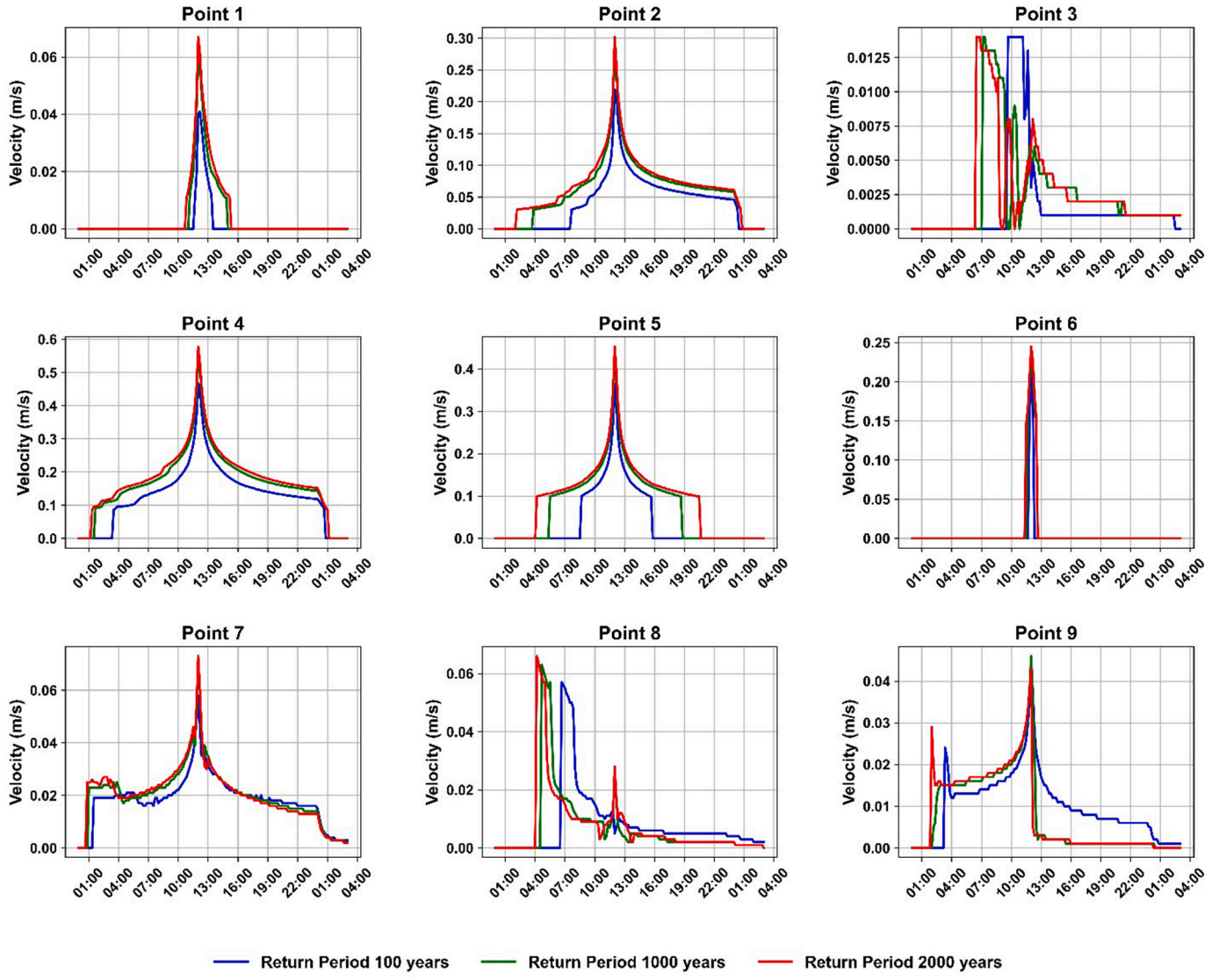

Fig. 18. Velocity profiles at nine sampling points.

hyetographs rather than observed hydrographs, the results indicate that iterative, nested RoG applications at the CH scale may be preferable.

This study shows that no significant major flood risk is present, and our results validate that the siting and spatial positioning adopted by the ancient engineers took into consideration inland flood events. However, while major flooding may not pose an immediate threat, other forms of water exposure remain a concern for these historic structures. The deterioration of mechanical properties due to water exposure poses considerable risks to the integrity and safety of limestone-built structures. Therefore, a thorough understanding of water-rock interactions and high-resolution flood analysis are essential for developing effective conservation and mitigation strategies, particularly for historically significant structures like the Temple of Apollo in Aegina. The combination of UAV photogrammetry with multi-scale RoG hydraulic models and mathematical models of material degradation, presented herein, enabled the development of (a) compressive strength and (b) elastic modulus reduction maps at the site level, and the identification of the most vulnerable CH structures of the particular site. These structures could witness up to a 10 % reduction of their compressive strength and elastic modulus during the flooding events considered in this study.

To quantify these impacts more precisely, the study yields the following key metrics:

- Precise hydraulic parameters: Specific inundation percentages (2–24 %), water volumes (92–1483 m^3), and velocity ranges (0.3–3.0 m/s) for different return periods.
- Quantified material degradation: Exact compressive strength reductions (0.00–10.42 %) and elastic modulus decreases (0.00–9.49 %) with corresponding inundation durations.
- Detailed mass loss calculations: Specific mass losses for individual structures ranging from 0.64 kg to 26.08 kg.
- Methodologically rigorous approach: Sub-centimeter photogrammetric accuracy (4–6 cm RMS error), multi-scale grid resolution specifications (5 m to 0.05 m), and numerical stability parameters.

Our proposed integrated modeling framework provides a reproducible framework for ex-ante flood risk assessment in CH contexts. Overall, the results demonstrate the necessity for combining large-scale hydrological data with fine-scale topographic surveys to inform robust conservation and mitigation strategies for CH sites.

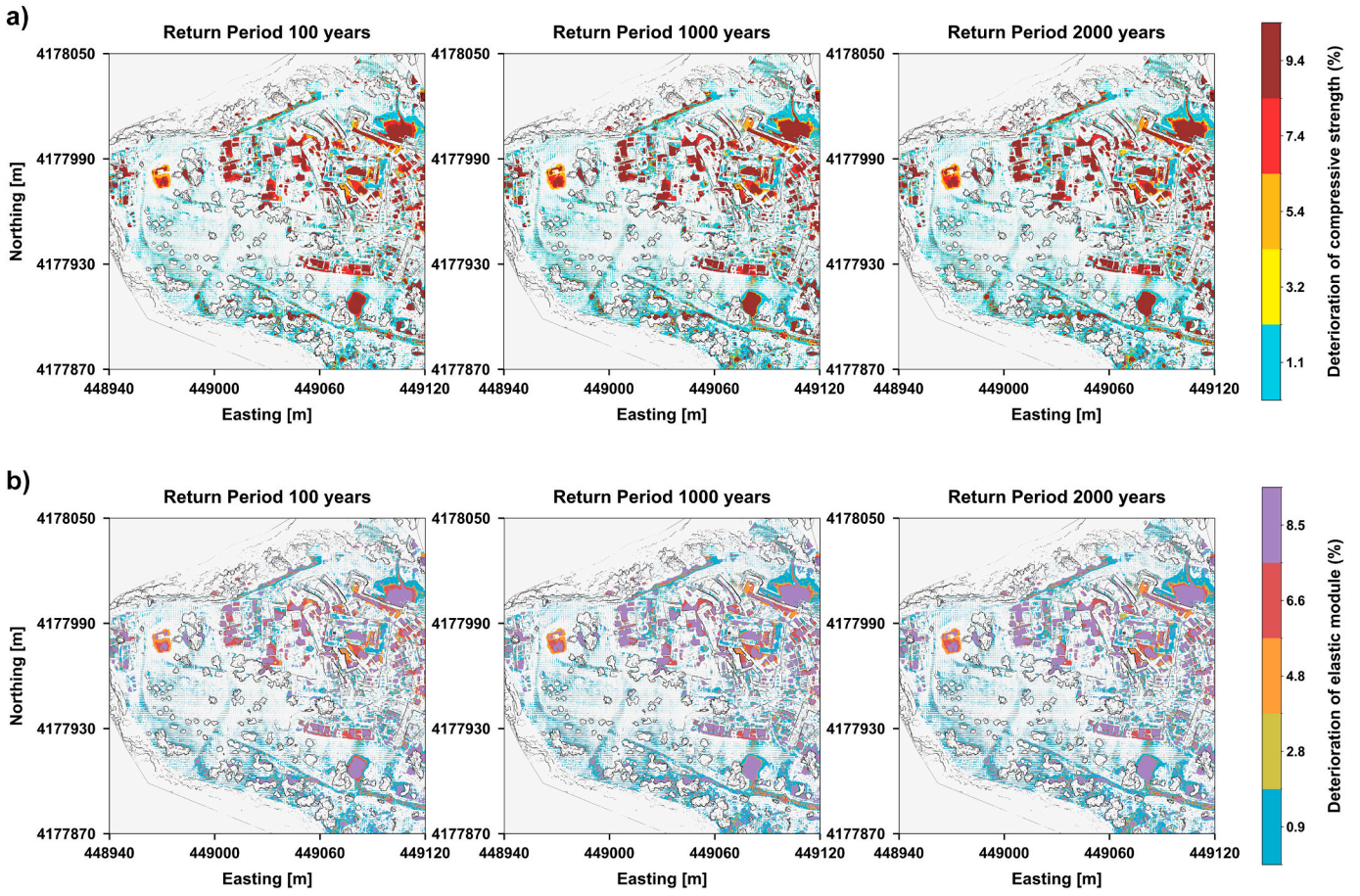

Fig. 19. Deterioration of the compressive strength (a) and of the elastic module (b) of the limestone structural material for the three return periods of 100-, 1000-, and 2000-years flooding events at the archeological site of Temple of Apollo in Aegina.

Table 2
Deterioration of compressive strength of elastic module of limestone from water inundation.

Inundation (%)	Duration of saturation (hours)	σ_c (MPa)	$R_{d,c}$ (%)*	E (GPa)	$R_{d,E}$ (%)
0	0	71.32	0.00	44.67	0.00
20	4.8	69.77	2.18	43.82	1.90
40	9.6	68.24	4.31	42.97	3.80
60	14.4	66.76	6.40	42.13	5.70
80	19.2	65.31	8.43	41.28	7.59
100	24	63.89	10.42	40.43	9.49

* $R_{d,c}$ stands for rate of deterioration of compressive strength and $Rd_{,E}$ stands for rate of deterioration of the elastic module.

Table 3
Initial remaining masses for the key representative structures of the CH site.

Structure	m_0 (kg)	$m_{r,t}$ (kg)	Mass loss (kg)
#1	13,986.97	13,985.57	1.40
#2	6442.15	6441.51	0.64
#3	65,938.63	65,932.03	6.59
#4	260,771.66	260,745.58	26.08

CRediT authorship contribution statement

M.J. Alexopoulos: Writing – original draft, Methodology, Investigation, Formal analysis, Data curation, Conceptualization. **T. Iliopoulou:** Writing – review & editing, Methodology, Investigation, Formal analysis, Conceptualization. **P. Modé:** Writing – original draft, Visualization, Methodology, Investigation, Formal analysis, Data curation. **D. Istrati:** Writing – review & editing, Supervision, Resources, Project administration, Methodology, Funding acquisition, Conceptualization. **C.C. Spyrakos:** Writing – review & editing, Project administration, Funding acquisition. **S. Soile:** Writing – original draft, Visualization, Resources, Project administration, Methodology, Formal analysis, Data curation. **S. Verykokou:** Writing – original draft, Project administration. **C. Ioannidis:** Writing – review & editing, Visualization, Resources, Project administration, Methodology, Funding acquisition. **D. Koutsoyiannis:** Writing – review & editing, Supervision.

Declaration of competing interest

The authors declare that they have no known competing financial interests or personal relationships that could have appeared to influence the work reported in this paper.

Acknowledgements

This work is based on procedures and tasks implemented within the project "Toolbox for assessing and mitigating Climate Change risks and natural hazards threatening cultural heritage—TRIQUETRA", which is a Project funded by the EU HE research and innovation program under GA No. 101094818.

Appendix A. Supplementary data

Supplementary data to this article can be found online at https://doi.org/10.1016/j.scitotenv.2025.180256.

Data availability

Data will be made available on request.

References

Alexopoulos, M.J., Dimitriadis, P., Iliopoulou, T., Bezak, N., Kobold, M., Koutsoyiannis, D., 2024. Effects of digital elevation model resolution on rain-on-grid simulations: a case study in a Slovenian watershed. Hydrol. Sci. J. 69 (11), 1468–1485. https://doi.org/10.1080/02626667.2024.2378487.

Andreadis, K.M., Wing, O.E.J., Colven, E., Gleason, C.J., Bates, P.D., Brown, C.M., 2022. Urbanizing the floodplain: global changes of imperviousness in flood-prone areas. Environ. Res. Lett. 17 (10), 104024. https://doi.org/10.1088/1748-9326/AC9197.

Annis, A., Nardi, F., Volpi, E., Fiori, A., 2020. Quantifying the relative impact of hydrological and hydraulic modelling parameterizations on uncertainty of inundation maps. Hydrol. Sci. J. 65 (4), 507–523. https://doi.org/10.1080/02626667.2019.1709640.

Arosio, M., Arrighi, C., Bonomelli, R., Domeneghetti, A., Farina, G., Molinari, D., Monteleone, B., Scorzini, A.R., Martina, M., 2024. Unveiling the assessment process behind an integrated flood risk management plan. Int. J. Disaster Risk Reduct. 112, 104755. https://doi.org/10.1016/J.IJDRR.2024.104755.

Arrighi, C., Brugioni, M., Castelli, F., Franceschini, S., Mazzanti, B., 2018. Flood risk assessment in art cities: the exemplary case of Florence (Italy). J. Flood Risk Manag. 11, S616–S631. https://doi.org/10.1111/JFR3.12226.

Baltas, E.A., Dervos, N.A., Mimikou, M.A., 2007. Technical note: determination of the SCS initial abstraction ratio in an experimental watershed in Greece. Hydrol. Earth Syst. Sci. 11 (6), 1825–1829. https://doi.org/10.5194/HESS-11-1825-2007.

Ben Moshe, L., Lensky, N.G., 2024. Geomorphological Response of Alluvial Streams to Flood Events during Base-Level Lowering: Insights from Drone-Based Photogrammetric Surveys in Dead Sea Tributaries. Remote Sens. 16 (8), 1346. https://doi.org/10.3390/rs16081346, 2024, Vol. 16, Page 1346.

Bermúdez, M., Zischg, A.P., 2018. Sensitivity of flood loss estimates to building representation and flow depth attribution methods in micro-scale flood modelling. Nat. Hazards 92 (3), 1633–1648. https://doi.org/10.1007/S11069-018-3270-7.

Blanch, X., Guinau, M., Eltner, A., Abellan, A., 2023. Fixed photogrammetric systems for natural hazard monitoring with high spatio-temporal resolution. Nat. Hazards Earth Syst. Sci. 23 (10), 3285–3303. https://doi.org/10.5194/NHESS-23-3285-2023.

Brokerhof, A.W., Van Leijen, R., Gersonius, B., 2023. Protecting built heritage against flood: mapping value density on flood Hazard maps. Water 15 (16), 2950. https://doi.org/10.3390/W15162950, 2023, Vol. 15, page 2950.

Brussee, A.R., Bricker, J.D., De Bruijn, K.M., Verhoeven, G.F., Winsemius, H.C., Jonkman, S.N., 2021. Impact of hydraulic model resolution and loss of life model modification on flood fatality risk estimation: case study of the Bommelerwaard, the Netherlands. J. Flood Risk Manag. 14 (3), e12713. https://doi.org/10.1111/JFR3.12713.

Cea, L., Costabile, P., 2022. Flood risk in urban areas: modelling, management and adaptation to climate change. A review. Hydrology 9 (3), 50. https://doi.org/10.3390/HYDROLOGY9030050, 2022, Vol. 9, page 50.

Colucci, E., Matrone, F., Noardo, F., Assumma, V., Datola, G., Appiotti, F., Bottero, M., Chiabrando, F., Lombardi, P., Migliorini, M., Rinaldi, E., Spanò, A., Lingua, A., 2024. Documenting cultural heritage in an INSPIRE-based 3D GIS for risk and vulnerability analysis. J. Cult. Herit. Manag. Sustain. Dev. 14 (2), 205–234. https://doi.org/10.1108/JCHMSD-04-2021-0068.

De Lucia, C., Amaddii, M., Arrighi, C., 2024. Tangible and intangible ex post assessment of flood-induced damage to cultural heritage. Nat. Hazards Earth Syst. Sci. 24 (12), 4317–4339. https://doi.org/10.5194/NHESS-24-4317-2024.

Ennouini, W., Fenocchi, A., Petaccia, G., Persi, E., Sibilla, S., 2024. A complete methodology to assess hydraulic risk in small ungauged catchments based on HEC-RAS 2D rain-on-grid simulations. Nat. Hazards 120 (8), 7381–7409. https://doi.org/10.1007/S11069-024-06515-2.

Erbach, T., 2025. Using cultural heritage in climate adaptation: fields of application and functions. Wiley Interdiscip. Rev. Clim. Chang. 16 (4), e70011. https://doi.org/10.1002/WCC.70011.

Fan, S., Song, Z., Xu, T., Zhang, Y., 2022. Investigation of the microstructure damage and mechanical properties evolution of limestone subjected to high-pressure water. Constr. Build. Mater. 316, 125871. https://doi.org/10.1016/j.conbuildmat.2021.125871.

Fatorić, S., Seekamp, E., 2017. Are cultural heritage and resources threatened by climate change? A systematic literature review. Clim. Change 142 (1–2), 227–254. https://doi.org/10.1007/S10584-017-1929-9.

Figueiredo, R., Romão, X., Paupério, E., 2020. Flood risk assessment of cultural heritage at large spatial scales: framework and application to mainland Portugal. J. Cult. Herit. 43, 163–174. https://doi.org/10.1016/J.CULHER.2019.11.007.

Figueiredo, R., Romão, X., Paupério, E., 2021. Component-based flood vulnerability modelling for cultural heritage buildings. Int. J. Disaster Risk Reduct. 61. https://doi.org/10.1016/J.IJDRR.2021.102323.

Giani, G., Rico-Ramirez, M.A., Woods, R.A., 2022. Are moments of rainfall spatial variability useful for runoff modelling in operational hydrology? Hydrol. Sci. J. 67 (10), 1466–1479. https://doi.org/10.1080/02626667.2022.2092405.

Ginzarly, M., Joshi, M.Y., Teller, J., 2024. A multidimensional framework for assessing cultural heritage vulnerability to flood hazards. Int. J. Herit. Stud. 30 (10), 1173–1192. https://doi.org/10.1080/13527258.2024.2378438.

Godara, N., Bruland, O., Alfredsen, K., 2024. Comparison of two hydrodynamic models for their rain-on-grid technique to simulate flash floods in steep catchment. Front. Water 6, 1384205. https://doi.org/10.3389/FRWA.2024.1384205.

Guan, M., Ahilan, S., Yu, D., Peng, Y., Wright, N., 2018. Numerical modelling of hydro-morphological processes dominated by fine suspended sediment in a stormwater pond. J. Hydrol. 556, 87–99. https://doi.org/10.1016/J.JHYDROL.2017.11.006.

Hariri, S., Weill, S., Gustedt, J., Charpentier, I., 2022. A balanced watershed decomposition method for rain-on-grid simulations in HEC-RAS. J. Hydroinf. 24 (2), 315–332. https://doi.org/10.2166/hydro.2022.078.

Iliopoulou, T., Dimitriadis, P., Koutsoyiannis, D., 2023. Pluvial flood risk assessment in urban areas: a case study for the archaeological site of the Roman agora, Athens. Heritage 6 (11), 7230–7243. https://doi.org/10.3390/HERITAGE6110379, 2023, Vol. 6, Pages 7230–7243.

Iliopoulou, T., Koutsoyiannis, D., Malamos, N., Koukouvinos, A., Dimitriadis, P., Mamassis, N., Tepetidis, N., Markantonis, D., 2024. A stochastic framework for rainfall intensity–time scale–return period relationships. Part II: point modelling and regionalization over Greece. Hydrol. Sci. J. 69 (8), 1092–1112. https://doi.org/10.1080/02626667.2024.2345814.

Ioannidis, C., Verykokou, S., Soile, S., Istrati, D., Spyrakos, C., Sarris, A., Akritidis, D., Feidas, H., Georgoulias, A.K., Tringa, E., Zanis, P., Georgiadis, C., Martino, S., Feliziani, F., Marmoni, G.M., Cerra, D., Ottinger, M., Bachofer, F., Anastasiou, A., Anyfantis, G.C., 2024. Safeguarding our heritage—the TRIQUETRA project approach. Heritage 7 (2), 758–793. https://doi.org/10.3390/HERITAGE7020037, 2024, Vol. 7, Pages 758–793.

Kim, J., Sung, H.H., 2024. Assessing flood risk of heritage sites in an urban area: impact of locational characteristics and historical context. Sustainability 16 (23), 10473. https://doi.org/10.3390/SU162310473, 2024, Vol. 16, page 10473.

Kumar, A., Biswas, S., Rallapalli, S., Shashwat, P., Balaji, S., Gupta, R., 2025. Micro-macro–scale flood modeling in ungauged channels: rain-on-grid approach for improving prediction accuracy with varied resolution datasets. J. Hydrol. 654, 132862. https://doi.org/10.1016/J.JHYDROL.2025.132862.

Li, H., Wang, J., Wang, X., Liang, W., Xu, G., Kang, Y., 2022. Influence of water saturation time on microstructure and mechanical properties of jointed limestone. Front. Earth Sci. 10, 922683. https://doi.org/10.3389/FEART.2022.922683.

Liang, L., Chen, Y., Gong, A., Sun, H., 2024. A modified geographical weighted regression model for better flood risk assessment and management of immovable cultural heritage sites at large spatial scales. J. Cult. Herit. 68, 276–286. https://doi.org/10.1016/J.CULHER.2024.06.006.

Malgwi, M.B., Ramirez, J.A., Zischg, A., Zimmermann, M., Schürmann, S., Keiler, M., 2021. A method to reconstruct flood scenarios using field interviews and hydrodynamic modelling: application to the 2017 Suleja and Tafa, Nigeria flood. Nat. Hazards 108 (2), 1781–1805. https://doi.org/10.1007/s11069-021-04756-z.

Miao, S., Cai, M., Guo, Q., Wang, P., Liang, M., 2016. Damage effects and mechanisms in granite treated with acidic chemical solutions. Int. J. Rock Mech. Min. Sci. 88, 77–86. https://doi.org/10.1016/J.IJRMMS.2016.07.002.

Nguyen, D.M.T., Do, T.N., Van Nghiem, S., Ghimire, J., Dang, K.B., Giang, V.T., Vu, K.C., Pham, V.M., 2024. Flood inundation assessment of UNESCO world heritage sites using remote sensing and spatial metrics in hoi an City, Vietnam. Ecol. Inform. 79, 102427. https://doi.org/10.1016/J.ECOINF.2023.102427.

Pavesi, L., Volpi, E., Fiori, A., 2024. Flood risk assessment through large-scale modeling under uncertainty. Nat. Hazards Earth Syst. Sci. 24 (12), 4507–4522. https://doi.org/10.5194/NHESS-24-4507-2024.

Pereira, S., Zêzere, J.L., Quaresma, I., Santos, P.P., Santos, M., 2016. Mortality patterns of hydro-geomorphologic disasters. Risk Anal.: Off. Publ. Soc. Risk Anal. 36 (6), 1188–1210. https://doi.org/10.1111/RISA.12516.

Prior, E.M., Michaelson, N., Czuba, J.A., Pingel, T.J., Thomas, V.A., Hession, W.C., 2024. Lidar DEM and computational mesh grid resolutions modify roughness in 2D hydrodynamic models. Water Resour. Res. 60 (7), e2024WR037165. https://doi.org/10.1029/2024WR037165.

Rocha, J., Duarte, A., Silva, M., Fabres, S., Vasques, J., Revilla-Romero, B., Quintela, A., 2020. The importance of high resolution digital elevation models for improved hydrological simulations of a Mediterranean forested catchment. Remote Sen. 12 (20), 3287. https://doi.org/10.3390/RS12203287, 2020, Vol. 12, page 3287.

Roldán-Valcarce, A., Jato-Espino, D., Manchado, C., Bach, P.M., Kuller, M., 2023. Vulnerability to urban flooding assessed based on spatial demographic, socio-economic and infrastructure inequalities. Int. J. Disaster Risk Reduct. 95, 103894. https://doi.org/10.1016/J.IJDRR.2023.103894.

Salazar, L.G.F., Figueiredo, R., Romão, X., 2024a. Flood vulnerability assessment of built cultural heritage: literature review and identification of indicators. Int. J. Disaster Risk Reduct. 111, 104666. https://doi.org/10.1016/J.IJDRR.2024.104666.

Salazar, L.G.F., Romão, X., Figueiredo, R., 2024b. A hybrid approach for the assessment of flood vulnerability of historic constructions and their contents. In: RILEM Bookseries, 46, pp. 1117–1133. https://doi.org/10.1007/978-3-031-39450-8_91.

Sesana, E., Gagnon, A.S., Ciantelli, C., Cassar, J.A., Hughes, J.J., 2021. Climate change impacts on cultural heritage: a literature review. WIREs Clim. Change 12 (4), e710. https://doi.org/10.1002/WCC.710.

Snelling, R., Rismanchi, B., Holzer, D., 2024. Integrating asset-specific flood vulnerability assessments with value-based preservation processes to develop the heritage building flood robustness toolkit. J. Cult. Herit. 66, 282–293. https://doi.org/10.1016/J.CULHER.2023.11.025.

Tamagnone, P., Lompi, M., Caporali, E., 2025. Preserving the past in a changing climate: an approach to assess the impact of urban flooding in cultural heritage cities. J. Flood Risk Manag. 18 (2). https://doi.org/10.1111/JFR3.70043.

Vásárhelyi, B., 2005. Statistical analysis of the influence of water content on the strength of the Miocene limestone. Rock Mech. Rock Eng. 38 (1), 69–76. https://doi.org/10.1007/s00603-004-0034-3.

Vulliet, C., Koci, J., Jarihani, B., Sheaves, M., Waltham, N., 2024. Assessing tidal hydrodynamics in a tropical seascape using structure-from-motion photogrammetry and 2D flow modelling. Estuar. Coasts 47 (2), 352–375. https://doi.org/10.1007/s12237-023-01288-6.

Wang, J.J., 2015. Flood risk maps to cultural heritage: measures and process. J. Cult. Herit. 16 (2), 210–220. https://doi.org/10.1016/J.CULHER.2014.03.002.

Zazo, S., Rodríguez-Gonzálvez, P., Molina, J.L., González-Aguilera, D., Agudelo-Ruiz, C. A., Hernández-López, D., 2018. Flood Hazard assessment supported by reduced cost aerial precision photogrammetry. Remote Sens. 10 (10), 1566. https://doi.org/10.3390/RS10101566, 2018, Vol. 10, page 1566.